SHEAR VELOCITY STRUCTURE FROM AMBIENT NOISE AND TELESEISMIC SURFACE WAVE TOMOGRAPHY IN THE CASCADES AROUND MOUNT ST. HELENS

A Thesis

Presented to the Faculty of the Graduate School

of Cornell University

In Partial Fulfillment of the Requirements for the Degree of

Master of Science

by

Kayla Jade Crosbie

Dec 2018

ABSTRACT

The location of Mount St. Helens on the cold forearc, 50 km trenchward of the main volcanic front, is contradictory to regional thermal models. To answer why Mount St. Helens is in this unusual position, a dense (10 km spacing) broadband seismic array with a large aperture (100 km) was deployed. Data from this array provide one of the first high-resolution tomographic images of the crust and upper mantle of a volcanic region. Using ambient noise and teleseismic surface waves, we make phase velocity maps and 3D images of shear velocity (*Vs*). These inversions image an anomalously fast mid-lower crust (3.95 $\pm$0.1 km/s) west and under Mount St. Helens (MSH). This is likely the Siletzia terrane, an accreted mafic igneous province. This high crustal velocity contributes to a weak forearc Moho, which has almost no *Vs* increase west of MSH (3.9 to 4.0 km/s) compared to an increase from 3.6 to 4.5 km/s (0.9 km/s) east of MSH. The mantle Vs is 4.0-4.2 km/s west of MSH, consistent with the weak Moho and likely due to hydration; however, the weak Moho is mostly due to the fast forearc crust. Also, a low *Vs* body (3.45-3.6 km/s) lies in the middle to lower crust between MSH and the main arc volcanoes of Mount Rainier and Mount Adams. This low velocity features is likely a hot region that may have melt in the mid-crust; and correlates with vent fields. Moreover, the boundaries of Siletzia and the weak forearc Moho lie precisely at MSH, and it is thought that these geologic boundaries influence magmatism.

BIOGRAPHICAL SKETCH

Kayla is the daughter of Jeanne Townley, Scott Townley, and Jeff Crosbie. She was raised in Gilbert, Arizona. She has four siblings, Brandon Crosbie, Nick Townley, Kaly Crosbie, and Philipp Zaviryukha. Kayla attended the University of Colorado at Boulder as an undergraduate, double majoring in Math and Physics, and earned a Bachelor of Arts in 2011. She came to Cornell University in fall of 2011, entering the Physics PhD program. She then transferred to the Earth and Atmospheric Sciences program in 2014. After graduating she plans to pursue illustration and live in Ithaca.

Dedicated to my mom, who is my constant support.

ACKNOWLEDGMENTS

All data are collected through the IRIS-PASSCAL Instrument Center, who provided invaluable field and management support. Numerous participants in iMUSH fieldwork 2014-16 made this project possible; we particularly acknowledge support from Cascade Volcano Observatory (S. Moran and R. Denlinger). All waveform data are archived at the IRIS Data Management Center. A. Foster provided an early version of the earthquake phase velocities used in initial tests. This project is funded by NSF grant EAR-1444275.

This thesis would not have been possible without the guidance from my advisor, Geoff Abers. His dedication to helping me propelled this project greatly. I also thank my minor advisor Katie Keranen for her encouragement and help throughout my graduate education. My gratitude goes out to everyone on iMUSH team that I did field work with, especially Carl Ulberg (University of Washington), Ken Creager (University of Washingont), and Seth Moran (USGS). I want to especially thank Roger Denlinger (USGS) for his help in the field, mentorship, and good stories of bushwhacking around Mount St. Helens in the rain at night. Thanks to Muawia Barazangi for all his encouragement and various snacks left at my desk. I'd like to thank my lab mates for their encouragement and solidarity, particularly Dana Peterson, Stephanie Nale, Cat Lambert, Nate Stevens, Michael Mann, Roque Soto Castaneda, and Doyeon Kim. Dana Peterson deserves the most thanks for being a great friend and a great person to bounce science ideas off of. Finally thanks to my mom and my partner Matt Bierbaum for their support and love.

TABLE OF CONTENTS

CHAPTER 1

1.1 Introduction

Subduction-related volcanism typically occurs when the top of the subducting plate reaches 100 km depth, and flux melting in the mantle wedge migrates through the crust, defining a narrow arc (Syracuse & Abers, 2006). However, crustal structures can be equally important in controlling the location of volcanism. Lower-crustal mush zones are purported to be the source for volcanoes (Annen et al., 2006; Behn & Kelemen, 2006; Tatsumi et al., 2008), and are a location for storage and assimilation of melt. Petrology at Mount St. Helens (MSH) and globally confirms that melt exists as a crystal-rich transcrustal plumbing system before transiently moving to shallow magma chambers (Blatter et al., 2017; Cashman et al., 2017; Claiborne et al., 2010). These lower crustal mush zones have been imaged (Hill et al., 2009; Ward et al., 2014; Delph et al., 2017); however, the locations on earth where this has been imaged are limited.

Volcanism in the Cascades typically occurs where the top of the subducting Juan de Fuca plate reaches 80-90 km depth (McCrory et al., 2012), similar to global systematics (Syracuse & Abers, 2006). MSH, the most active Holocene volcano in the Cascades, unusually lies 50 km west of the main arc (Figure 1.1; Figure 1.2). The melt transport pathway is not understood, since the forearc heat flow is markedly low, 37 ± 10 mW/m^2 compared to 80 ± 20 mW/m^2 in the arc, and MSH is located within this cold the forearc (Figure 1.3; Blackwell et al. 1990; Wada and Wang, 2009; Pollack et al., 1993). Since the location of MSH is inconsistent with the cold temperatures in the forearc, this implies that crustal structures are important for the source of melt.

The region has been previously studied geophysically with lower resolution arrays or only focused on the upper-crustal magma systems, including passive seismic studies (Lees and Crosson, 1989; Waite and Moran, 2009; De Siena et al., 2014; Flinders and Shen, 2017; Wang et al., 2017) and active seismic studies (Parsons et al., 1998; Kiser et al., 2016). The middle and lower crust have been particularly undersampled at wavelengths less than volcano spacing (50 km). This study images the lower crust to get a complete picture of the volcanic plumbing system of MSH.

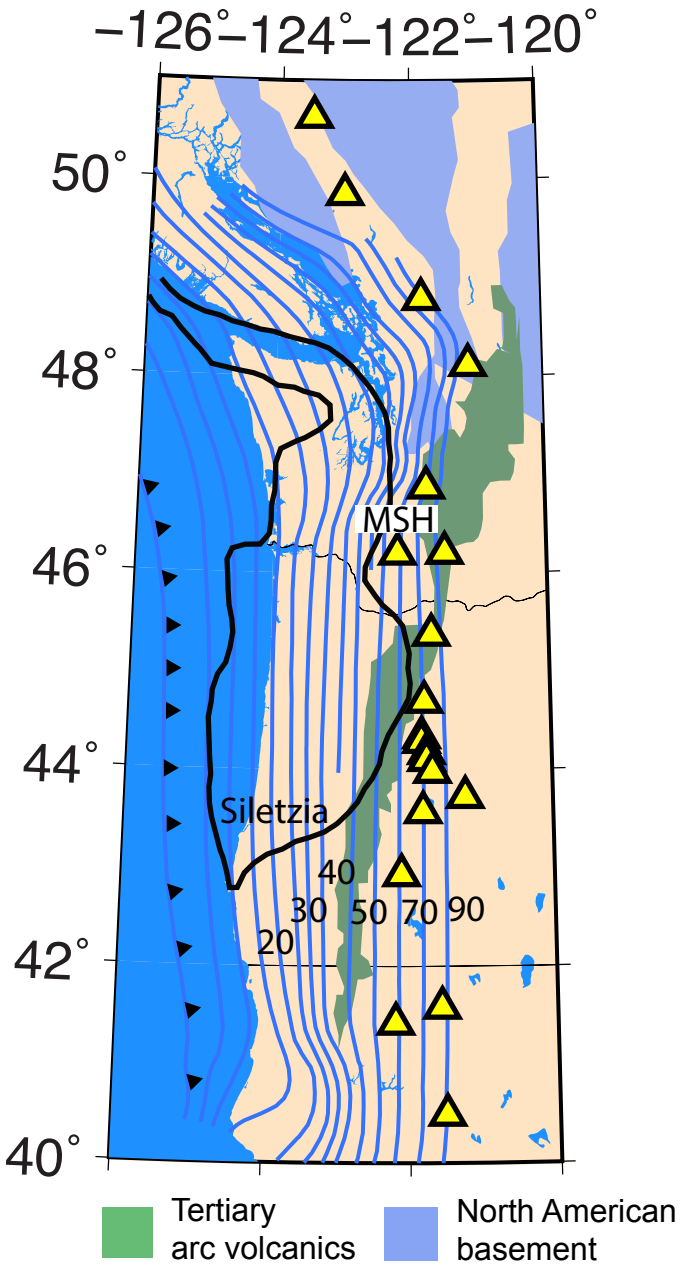

Figure 1.1: Regional setting: The Cascades. Black outline is Siletzia terrane (Wells et al., 2014), green is the Tertiary Cascades arc volcanics and blue is North American basement (Reed et al., 2004; Wheeler et al., 2004). Blue lines are top of subducting slab (McCrory et al., 2012), and yellow triangles are arc volcanoes (Hildreth et al., 2007). Brown box is the local region for **Figure 1.2.**

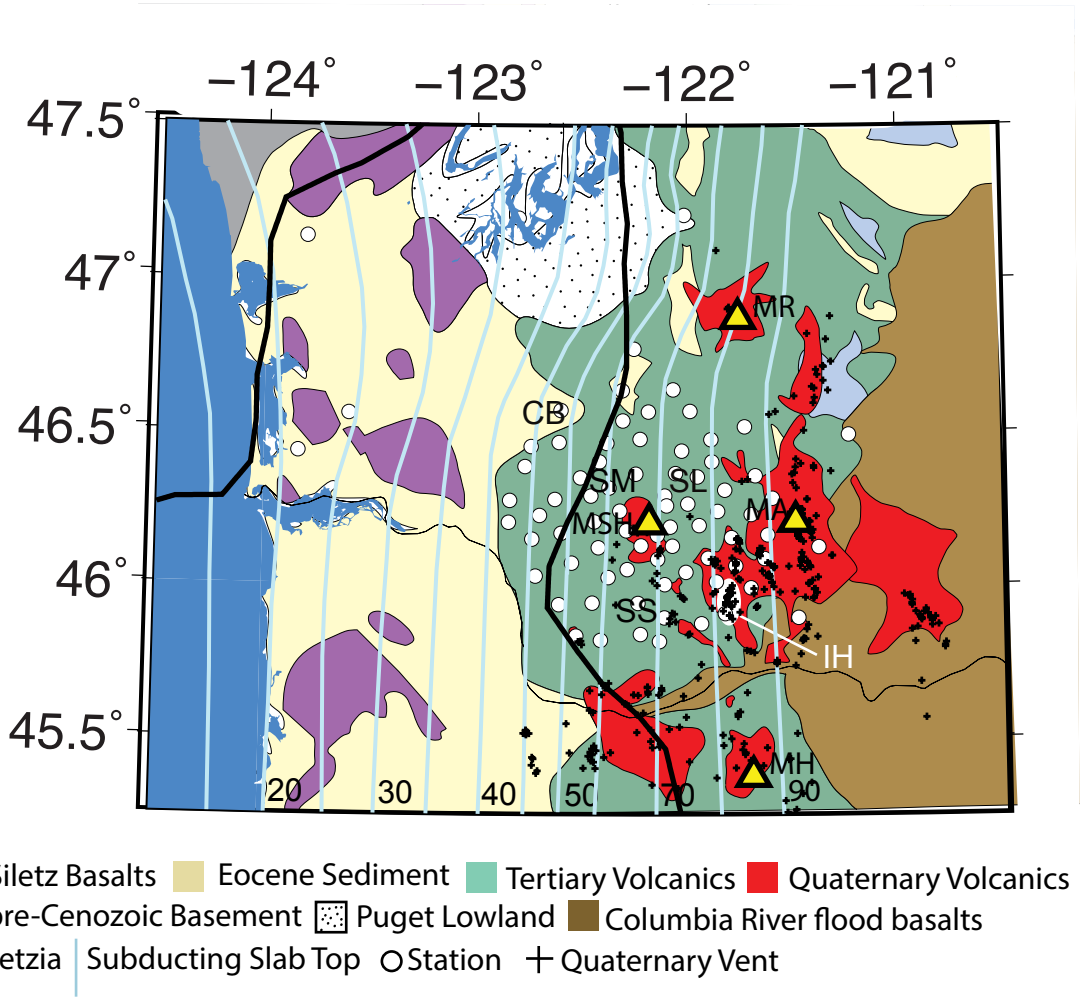

Figure 1.2: Cascadia near Mount St. Helens (MSH), Mount Adams (MA), Mount Rainier (MR), and Mount Hood (MR) (yellow triangles; Hildreth et al., 2007). White circles are seismic stations from iMUSH, TA, and UW array. Black crosses are Quaternary vents (Hildreth et al., 2007). Yellow line is magnetic outline of Siletzia (Wells et al., 2014). Top of subducting slab in light blue (McCrory et al., 2012). Simplified geology from Sisson et al. (2014): (green) Tertiary volcanics, (light yellow) Eocene sandstones and silts, (purple) Siletz Basalts, (brown) Columbia River flood basalts, (red) Quaternary volcanics, (light blue) pre-Cenozoic basement, (stippled white) Puget lowland. Sedimentary basins and plutons labeled: (CB) Chehalis Basin, (SM) Spud Mountain pluton, (SL) Spirit Lake pluton, and (SS) Silver Star pluton. 50 mafic vents make up Indian Heaven (IH; white oval) (Hildreth et al., 2007).

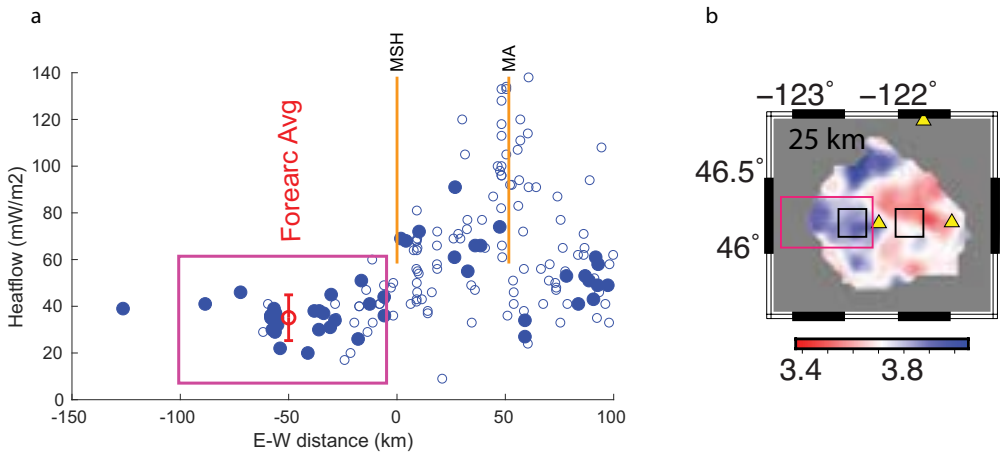

Figure 1.3: a: Heat flow data (Pollack et al., 1993, as compiled in van Keken et al., 2018) for an E-W transect through MSH, pink box denotes area where forearc heat flow average is taken. **b:** Map showing regions averaged for **Fig. 1.13**, the east and west Vs averages (black squares) and the heat flow forearc average (pink box). Open circles are 60 km north of MSH and solid are at the latitude of MSH. Horizontal axis is zero at MSH summit.

We use the iMUSH seismic array (imaging the Magma Under St. Helens) to address the effect of deeper crustal geology on the volcanic plumbing system. The iMUSH project (Kiser et al., 2016; Hansen et al., 2016; Wang et al., 2017; Bedrosian et al., 2018; Ulberg et al., in prep; Mann et al., subm.) gives one of the highest resolution 3D images of deep structure beneath MSH to date. This paper applies frequency-domain methods of measuring Rayleigh wave phase velocity from ambient noise to resolve features as small as one wavelength (Ekström et al., 2009; Luo et al., 2015), optimizing use of the array. In addition, surface wave earthquake Helmholtz tomography (Janiszewski et al., 2018; Jin & Gaherty, 2015) provides complementary mantle imaging and the results are incorporated into this study. Fundamental-mode Rayleigh phase velocities from both methods are inverted for shear velocity (*Vs*), which constrains geologic features from the subducting slab to the surface. These data reveal a strong control on volcanic architecture from pre-existing crustal structure, including a strong role of the mafic Siletzia terrane on possible volcano location and the forearc Moho discontinuity. Low shear-wave velocities in the middle-lower crust

between MSH, Mount Adams, Mount Rainier, and Indian Heaven can only be explained with partial melt, and so the melt source for MSH may be towards the arc from a large hot region, similar to Hill et al., 2009 and Bedrosian et al., 2018.

1.2 Tectonic Overview

Volcanism in the Cascades is a product of subduction of the Juan de Fuca plate beneath the North American Plate. This subduction zone is one of the youngest and hottest globally (Hyndman and Wang, 1993; Syracuse et al., 2010), with the spreading ridge less than 250 km from the volcanic arc. Because Cascadia is one of the hottest subduction zones it is one of the only subduction zones with sufficient slab dehydration at shallow depths to produce a fully hydrated forearc (Abers et al., 2017). This high level of hydration is thought to make the continental Moho vanish in the forearc, as discussed below, because serpentinites have much lower wavespeeds than typical peridotite (Bostock et al., 2002; Brocher et al., 2003). As a result, a weak-to-absent Moho serves as a proxy for low temperatures in the uppermost mantle. Heat flow is significantly less in the forearc mantle (37 mW/m^2 compared to 80 mW/m^2), and these lower temperatures allow for the stability of serpentinite (Wada and Wang, 2009). Therefore, the Moho vanishing in the forearc is primarily a thermal effect.

Beneath the Oregon and Washington coast ranges, the basement consists of accreted Siletzia terrane of Eocene submarine basalts and gabbros (Duncan, 1982), which was an oceanic plateau that collided with North America in the Eocene (Wells et al., 2014). The eastern limit is not observed geologically, and is thought to either be west of MSH (Wells et al., 2014) in eastern Washington (Schmandt & Humphreys, 2011). The basement to the east of Siletzia is a Mesozoic and Paleozoic mix of up to 50 different terranes that are a range of oceanic, volcanic and continental affinities that have metamorphized (Coney et al., 1980) and are fairly felsic (Valley et al., 2003). Partly burying the Siletzia terrane and the arc igneous rocks are quartz-rich sands and silts from fluvial, deltaic, and shallow-marine sediments deposited in the Eocene. These sediments make up the Puget Group in southwest Washington (Buckovic, 1979; Heller et al., 1985). The early Tertiary

Cascades run north-south in a wide band where the Cascades used to lie (Sisson et al., 2014). In the mid-Miocene there was widespread volcanic activity that covered a broad zone across most of western Oregon and Washington with the Columbia River flood basalts (Kasbohm & Schoene, 2018). These geologic features are displayed in Figure 1.2.

The axial belt of the Cascades from southern Washington to northern Oregon include five andesite-dacite centers: Jennies Butte, Goat Rocks, Mount Adams, Mount Rainier, and Mount Hood, as well as 15 basaltic shields and 130 smaller quaternary vents which are predominately basaltic and basaltic andesite with very few dacites and andesites (Figure 1.4) (Clayton, 1980; Smith, 1993). In the forearc, west of the Quaternary axis, lie three volcanoes: Mount St. Helens (MSH), 50 closely located mafic vents that make up the Indian Heaven Volcanic Field (IH), and a scattering of forearc vents in the Portland region. Quaternary vents near MSH are displayed in Figure 1.4. There is laterally broad cross-arc volcanism from the Boring lava fields to the Simcoe mountains (Hildreth, 2007). These volcanoes require a variety of sources, some from deeper in the mantle than others (Leeman et al., 2004). The compositional diversity in the basalts across the Cascades shows that there is a strong contribution from subcrustal processes (Leeman et al., 1990). Because the Cascades subduction margin is so hot, H_20 is getting down to the melt region creating basalts melts with up to 3.4 wt% H_20 (Walowski et al., 2015).

MSH is a dacitic volcano and recently one of the most active volcanoes in the Cascades. It came into existence around 300ka and remained quiet until after 28 ka (Clynne et al., 2005). In the last 28 kyr it has erupted 75 ± 15 km^3 of magma (Crandell, 1987; Scott, 1988,1989; Mullineaux, 1996). There were some basaltic eruptions during the Castle Creek eruptive period (2200-1770 years ago) suggesting a mantle source (Hoblitt et al., 1980). 8000 years ago basaltic andesites erupted from the nearby vents (Hammond and Korosec, 1983) some trending along the St. Helens seismic zone (Weaver et al., 1987). The most recent eruption (2004-2008) was the richest in silica in the past 500 years (Pallister et al., 2008). Experiments indicate that the dacites at MSH were generated at deep crustal pressures (700-900 MPa, 20-35 km) at high temperatures (925°C) with high H_2O concentrations (3 wt%), likely sourced from a basaltic andesite (Blatter et al., 2017).

IH is located 30 km southwest of Mount Adams and is a 450 km^2 basaltic volcanic field, with 50 coalescing vents that are mainly mafic monogenetic volcanoes (Hammond and Korosec, 1983; Korosec, 1989). They have been erupting from the middle Pleistocene to the Holocene, with the last eruption 9 kya having an output of 0.9 km^3 (Mitchell et al., 1989). 80 percent of the total 60-80 km^3 erupted has been basalt, making it one of the largest volumes of Quaternary basalt in the Cascades (Hildreth, 2007). The 150 forearc Quaternary vents (the Boring Volcanic Field) are spread as far as 90 km west of the main arc axis (Allen, 1975; Conrey et al., 1996).

The forearc is interesting not only because of its anomalously high level of volcanism, but also because of its absence of a Moho discontinuity, in contrast to the strong Moho discontinuity in the arc. The absence of a Moho was observed in receiver functions in the southern Cascades (Bostock et al., 2002) and was thought to be due to the slow mantle velocities from a hydrated serpentinized mantle wedge. In active source studies, there was a weak PmP reflection in the forearc in multiple locations in the Cascades, from Vancouver Island to central Oregon (Brocher et al., 2003). Higher resolution active source study also showed a weak PmP reflection in the forearc that sharply transitioned to a strong PmP reflection right at the longitude of MSH (Hansen et al., 2016). Other geophysical studies in the Cascades (Blakely et al., 2005; Shen et al., 2013) support the observation of a hydrated mantle wedge, by imaging low velocities in the forearc mantle wedge.

Past seismic studies have mostly imaged the upper magma chamber and have limited resolution in the lower crust, including passive source (Lees and Crosson, 1989; Waite and Moran, 2009; De Siena et al., 2014; Flinders and Shen, 2017; Wang et al., 2017) and active seismic studies (Parsons et al., 1998; Kiser et al., 2016). Mount St Helens has been further studied with magnetotelluric imaging (Stanley et al., 1987; Hill et al., 2004). The magma chamber is seismically imaged to be 6-16 km, 5.5-8 km, between the surface and 6 km deep in Lees and Crosson, 1989, Waite and Moran, 2009 and De Siena et al., 2014 respectively. Some suggest there is a large region of partial melt in southeastern Washington between MSH, Mount Adams, and Mount Rainier in magnetotelluric imaging (Hill et al., 2004) and seismic imaging (Flinders and Shen, 2018). Alternatively, previous magnetotelluric imaging attributed this large conductive feature to be marine sedimenta-

ry rocks (Stanley et al., 1987). Kiser et al. (2016) suggests that the melt source of MSH is near the Moho, southeast of MSH where a low-*Vp* anomaly is imaged. This is to date the highest resolution image of the lower crust at MSH, until this paper.

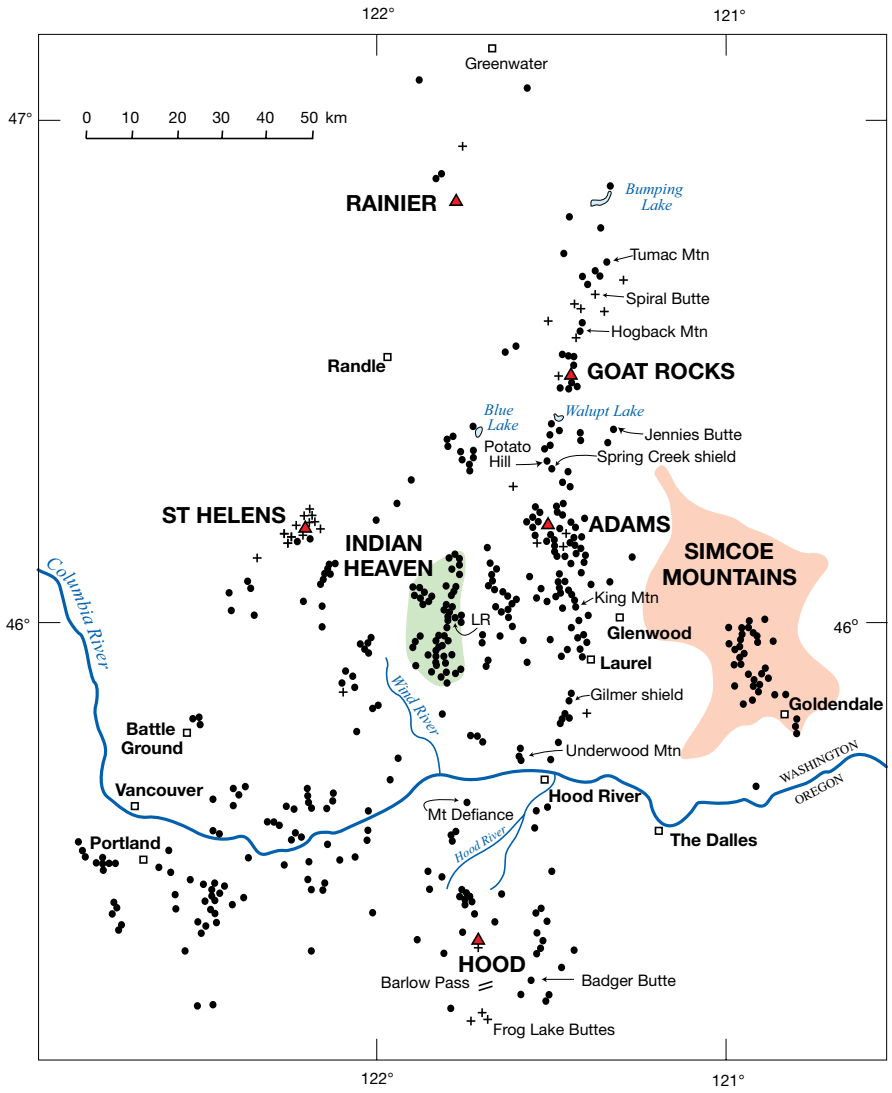

Figure 1.4: The 412 Quaternary volcanic vents of the Rainier-to-Hood segment of the Cascade arc, Figure 8 from Hildreth (2007). Two coloured fields depict limits of vent distributions that define the Indian Heaven Volcanic Field (middle Pleistocene and younger) and the Simcoe Mountains Volcanic Field (4.5-0.6 Ma), within which only ~35 Quaternary vents are indicated. Dots represent volcanoes of basaltic to andesitic composition and crosses are dacitic to rhyolitic. Triangles are major edifices.

2 Data, Methods, and Results

2.1 Data

We analyze broadband data from all 70 broadband instruments of the iMUSH array deployed between July 2014 and August 2016, and 13 additional broadband stations within 100 km of MSH from permanent or temporary arrays (Figure 1.2). The iMUSH array has a 100 km diameter centered on MSH with an average station spacing of 10 km. In this study we use vertical-component signals only and we use a continuous, 1 sample-per-second data stream or, where unavailable, decimate data to this sample rate. Phase velocity data at the lower frequencies (0.02-0.05 Hz) are taken from Janiszewski et al. (2018).

2.2 Measuring phase velocities

2.2.1 Phase velocity measurements from ambient noise.

Ambient noise is cross-correlated between seismic station pairs to extract the wavefield travelling between the two stations (Aki, 1957; Shapiro & Campillo, 2004). This signal is dominated by the fundamental-mode Rayleigh wave (Ekström et al., 2009). Twelve months of seismic traces are preprocessed using a methodology similar to Bensen et al. (2007) as detailed by Calkins et al. (2011), to produce 600 s long correlograms. Phase velocities are calculated from the correlograms in the frequency domain using methods based on Ekström et al. (2009) and Jin et al. (2015). Following Jin et al. (2015), the real part of the Fourier spectrum of the cross-correlation is fit to a smoothly varying phase velocity $c(\omega)$ at angular frequency ω, as a spline with knots every 0.02 Hz from 0.02 to 0.2 Hz, with extra knots at 0.01 and 0.05 Hz (Figure 2.1). The fitting procedure simultaneously fits the observed spectrum, minimizes the curvature of the dispersion curve, and enforces a negative slope $dc(\omega)/d\omega$. Although we fit frequencies < 0.04 Hz to improve numerical stability, the short interstation distances relative to wavelength are unable to resolve spatial variations in phase velocity at those low frequencies, and they are not analyzed further.

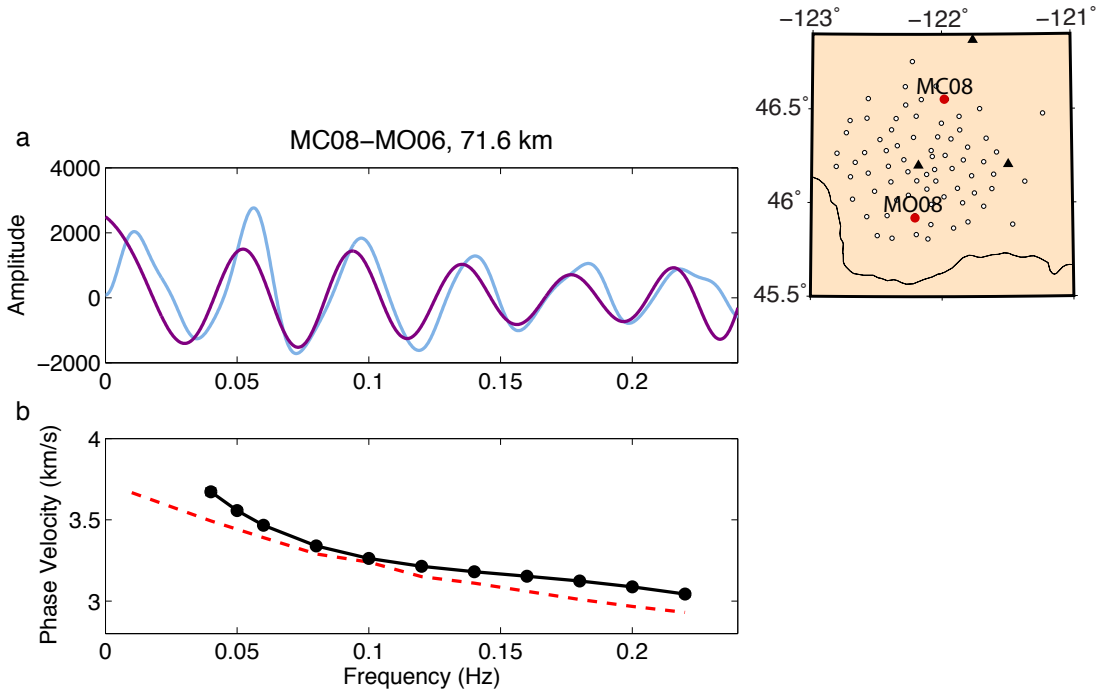

Figure 2.1: Example of phase velocity measurement for the station pair MC08-MO06 (labeled in **inset**), with path separation of 71.6 km. **a:** Real part of correlogram spectrum (blue) and fit (purple). **b:** Corresponding phase velocity fit (solid line, dots at tabulated frequencies) and prediction from starting model (dashed line).

The 83 stations provide between 681 and 2356 useable station pairs at each frequency after quality control measures, with more useable pairs for higher frequencies. At each frequency, measurements at distances of 1-2 cycles, 2-3 cycles, and > 3 cycles are grouped, and phase velocities exceeding three median absolute deviations from the median for each group are discarded. Appendix A.1 shows examples of this quality control procedure for two frequencies and the resulting phase velocity measurements in map view. Paths for station spacing less than one cycle (distance/wavelength) are not usable because the phase velocity measurements will be inaccurate, although

this frequency-domain measurement method is successful at 1-3 wavelengths unlike common time-domain methods (Calkins et al., 2011). The different criteria in number of cycles chosen was due to the large wavelength of low frequency waves approaching the array aperture size. Most of the data would be omitted if the criteria are too strict. The phase velocities for each pair-wise path are plotted at the midpoint of the path between stations. The map in Figure A.1c shows coherent patterns in the velocity structure to test that the inversion results are similar to the raw data. The ray density map (Figure A.1d) shows that rays are most dense in the center of the array, decreasing in density with radius from MSH.

2.2.2 Earthquake Surface Wave Phase Velocities

We incorporate measurements of fundamental-mode Rayleigh wave velocity for frequencies 0.02-0.05 Hz from earthquake sources from a prior study (Janiszewski et al., 2018). These phase-velocity maps are calculated via Helmholtz-equation inversion from Rayleigh waves sampled by arrays of stations; these methods provide focusing-corrected phase velocity maps across the array for individual earthquakes (Jin and Gaherty, 2015; Lin and Ritzwoller, 2011). Phase velocity uncertainties for these measurements are calculated from the standard deviations of all individual earthquake phase-velocity maps at each node, after outlier removal. At 0.05 Hz ambient noise phase velocities and regional earthquake phase velocities are combined with a cosine-taper window as described in Appendix A.2.

2.2.3 Network-averaged phase velocities and shear-wave velocities

To derive a S-wave velocity (*Vs*) model with depth *z* (Figure 2.2; Appendix Table D.1), a network-averaged dispersion curve $c(\omega)$ is found. The ambient noise average phase velocities are found by averaging all station-pair phase velocities at > 0.05 Hz. The earthquake-derived phase velocities at <0.04 Hz are averaged in the region where ambient noise tomography has ray coverage. At 0.05 Hz, where both data types (earthquake-derived and ambient noise) provide infor-

mation, we equally average the phase velocities from the two datasets. This composite dispersion curve provides a starting phase velocity for generating phase velocity maps (Figure 2.2d), and is used to produce reference *Vs(z)* model. The dispersion curve is also compared to estimates made by beamforming (Figure 2.2c; purple squares) following the method of Harmon et al. (2008), as discussed in the Appendix (Section B).

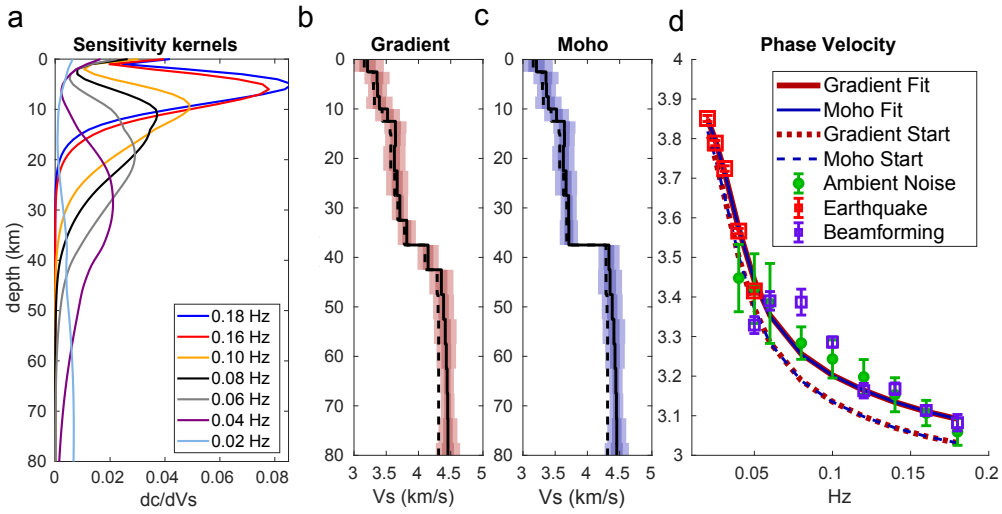

Figure 2.2: The array-averaged *Vs* with and without a Moho for the 1D inversions, and corresponding average dispersion curve. **a:** Sensitivity kernels, which show sensitivity of fundamental-mode Rayleigh phase velocity to *Vs* variation with depth, at each frequency. Calculated from the gradient starting model. **b:** The 1D *Vs* models for a gradient Moho. The starting model (dashed black) is a moving average of the group 1 average *Vs* from Obrebski et al. (2015). Solid black line is the 1D *Vs* model result. The Monte Carlo uncertainties shown in solid red, with 1-sigma and 2-sigma uncertainties (shading) derived from the standard deviations. **c:** The 1D *Vs* models with a starting model with a discontinuous Moho at 37.5 km depth; format same as panel **c. d:** Array-average phase velocity (symbols), along with predictions for both the gradient model (red) and Moho start model (blue). Red symbols shows average dispersion curve is from regional surface wave earthquake tomography phase velocities (Janiszewski et al., 2018) and green show ambient noise average. Purple squares: average velocities from the beamforming method; see Appendix B. Dashed lines are the phase velocity predictions from the starting models for gradient inversion (red) and Moho inversion (blue), corresponding to dashed lines in panels **b** and **c** respectively.

From the network-averaged $c(\omega)$, a 1D shear velocity model $Vs(z)$ is inverted for, using the iterative nonlinear method of Herrmann and Ammon (2004). A simple $Vs(z)$ model from Obrebski et al., (2015) (group 1 average Vs), is smoothed and used as the starting model (dashed blue line in Figure 2.2b). Layer thicknesses are 2.5 km at depths less than 22.5 km and 5 km between 22.5 and 112.5 km depth, underlain by a constant-velocity half space. This inversion imposes a first-derivative smoothing constraint; at sequential iterations the damping value is progressively decreased from 8.0 km^{-2} to 0.5 km^{-2} until the variance converges. Initial damping values are comparable to the largest singular value of the inversion, 8.37 km^{-2}, while the final ones are 16x smaller. The result from this inversion is referred to as the gradient model, since Vs varies smoothly with z with no discontinuities. Throughout the text we compare inversions using this gradient model with a similar model featuring a Moho discontinuity at 37.5 km depth across which smoothing constraints are removed. The Moho discontinuity is set to 0.6 km/s by perturbing the same starting model (dashed line Figure 2.2c); we refer to this $Vs(z)$ result as the Moho model (solid line Figure 2.2c).

Uncertainties (shading Figure 2.2b-c) are evaluated through Monte Carlo simulations in which 100 inversions as described above are repeated, randomly perturbing the starting model ±10% at 7 reference depths and interpolating between them. The reported uncertainty is the one-sigma standard deviation of the 100 models after removing outliers (solutions with an error exceeding 20% of the median or greater than a perturbation of 0.3 km/s). Both models and their uncertainties are given in Appendix Table D.1.

2.3 Phase velocity maps from ambient noise.

At each frequency the phase velocities measured for all station pairs are inverted for two-dimensional maps of phase velocity (Figure 2.6). This tomographic inversion (theory in Appendix C.2) solves for perturbations to phase slowness, $1/c(\omega)$ relative to a starting value as described above, at nodes every 5 km x 5 km, and treats station-pair measurements as travel times (distance/velocity) to approximately linearize the inversions. These inversions use finite frequency kernels

(Lin & Ritzwoller, 2010; Zhou et al., 2004), approximated to include only the inner two Fresnel zones where finite-frequency effects are most significant. For the iMUSH dataset the path lengths are short relative to wavelengths so finite frequency effects are pronounced. Tomographic inversions are stabilized via a first-derivative smoothness constraint and a weak model norm damping to stabilize undersampled regions, following standard damped least squares methodologies (Menke, 1989). This approach leads to two regularization parameters, one controlling smoothing (γ) and one controlling the norm damping (ε), with $\varepsilon << \gamma$ so that the norm damping has minimal effect except where data are largely absent. The parameter γ was determined by choosing a value that gave a local minimum in the generalized cross-validation (GCV) function (Inoue et al., 1990; Yao & Robert, 1999) (Appendix C.1). To calculate the GCV function, the inversion is repeated after omitting 100 different subsets of the data and calculating the misfit between the omitted data and its predicted values based on the fit to the remaining data. The γ value is determined in this way at 0.06 Hz and 0.18 Hz, and linearly interpolated and extrapolated to other frequencies (Appendix Table C.1).

Formal one-sigma uncertainty for the ambient noise tomography is calculated as part of the inversion following a standard least-squares approach (Menke, 1989), scaled to the root mean squared residuals for individual station pairs as an estimate of measurement uncertainty, plotted for 0.18 Hz and 0.06 Hz (Figure 2.3a-b). Uncertainties for phase velocity maps from earthquake surface waves are discussed in section 2.2.2.

2.4 Inversion for Shear Velocities (*Vs*)

At each 5 km by 5 km node, the phase velocities from all the single-frequency maps generate a dispersion curve $c(\omega)$ for that node. These curves are then inverted for $Vs(z)$ at that node with the same method as described in Section 2.2.3, except that the starting model for individual nodes is now set to the network-average gradient model. Ambient noise data are used at ≥ 0.05 Hz and earthquake data are used at ≤ 0.05 Hz. At 0.05 Hz the data are combined within the network and earthquake data alone are used outside it, as described in Appendix A.2. To balance the relative

weights of the different data types in the *Vs(z)* inversions, uncertainties for earthquake-based *c(ω)* were multiplied by five to be on average similar to the ambient noise uncertainties; these uncertainties are calculated with different assumptions so absolute levels are not directly comparable. In addition, the earthquake phase velocities should have lower resolution than the ambient noise phase velocity maps owing to the lower frequencies and sparser seismic array, so reweighting prior to vertical (*Vs*) inversion partly compensates for varying lateral resolution. Since it is expected that the difference in velocity across the Moho varies from strong in the east to nonexistent in the west (Hansen et al., 2016; Mann et al., 2017; subm.), inversions were run with both the network-average gradient and Moho model (Section 2.2.3; Figure 2.2b-c).

2.5 Results

2.5.1 Phase Velocity Results

2.5.1.1 Uncertainty

Formal one-sigma uncertainties for the ambient noise tomography phase velocity maps are 0.02-0.04 km/s within the region of best resolution (contours on Figure 2.3d-e). Formal uncertainties are slightly lower at higher frequencies; at 0.18 Hz uncertainty is 0.02-0.03 km/s and for 0.06 Hz it is 0.035-0.045 km/s. As a test, we also bootstrap the phase velocity inversion with randomly resampled sets of station pairs for 1000 bootstrap trials. Within the area of best resolution, the standard deviation of the bootstrap trials (estimate of uncertainty) is slightly lower than the formal error, by a factor of 1.36 at 0.06 Hz and 1.25 for 0.18 Hz. This suggests that formal errors slightly overestimate uncertainty, but are similar in magnitude. The formal one-sigma uncertainties for earthquake surface wave phase velocities (Figure 2.3c) are 0.007-0.015 km/s, calculated as described above. For the *Vs* inversions, earthquake-based phase velocity errors are scaled up by 5 as discussed above.

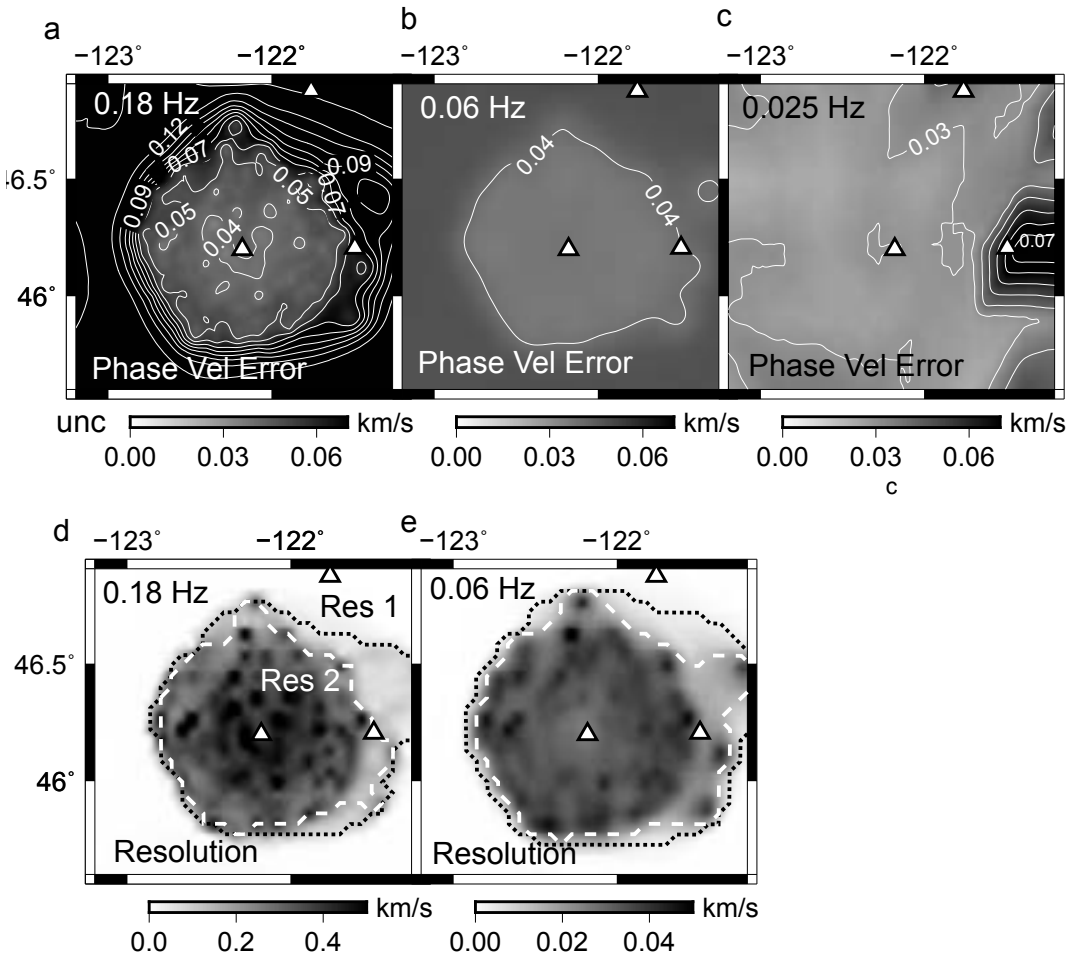

Figure 2.3: a-b: Formal uncertainty, as described in text, from phase velocity tomography from ambient noise at 0.180 and 0.060 Hz, and (**c**) from surface wave earthquake tomography at 0.025 Hz. **d,e:** Diagonals of resolution matrix for phase velocity inversions at 0.18 and 0.06 Hz. Resolution contour 1 denotes resolution diagonals greater than 1/25, and contour 2 denotes resolution greater than 1/5 the maximum. Uncertainties are reported as 1-σ.

2.5.1.2 Resolution and Recovery Tests

To evaluate lateral resolution of the phase velocity images we conduct a series of recovery tests on artificial data. Tests include checkerboard recovery and recovery of feature that resemble those we interpret. In each test, the synthetic data is solved for with the kernel from the given block model, and this data is input into the inversion with the same damping parameters as the real inversion process. Separately we evaluate recovery in the vertical inversions for *Vs*. Full three-dimensional recovery tests would involve full-waveform synthesis of Rayleigh waves from complex 3D structures and are beyond the scope of this paper.

First, we investigate the ability of these data to recover sharp lateral velocity steps across the array, such as seen in the mid-lower crust (Figure 2.4). These tests attempt to recover an east-west velocity step beneath the center of the array, set to 10%. The amplitude of this step is recovered 100 % at most frequencies. The transition between slow and fast velocities increases from a 10 km wide zone at 0.18 Hz to 30 km wide at 0.05 Hz, in both cases about half a wavelength. This test shows that wavelength rather than instrument spacing is limiting resolution within the array, emphasizing the importance of using finite-frequency kernels in the 2D inversion to have the highest resolution possible.

Checkerboard tests are conducted on the inversions for phase velocity with anomalies varying ±10% in $c(\omega)$ between blocks, for two block sizes of 15 and 50 km (Figure 2.5). A 50 km x 50 km anomaly has 100% amplitude recovery at 0.18Hz and 90% amplitude recovery at 0.05 Hz. The 15 km x 15 km blocks have up to 88% amplitude recovery at 0.18 Hz and only 10% recovery at 0.05 Hz. These tests demonstrate that the inversion recovers features of a size approximately equal to the wavelength of the fundamental-mode Rayleigh waves for each frequency. The area of best resolution, outlined where the diagonals of the resolution matrix at a central frequency, 0.1 Hz, drop to 1/5 their maximum value, is used to mask the shear velocity maps.

Further feature recovery tests are explored to see if small bodies such as melt zones or magma chambers can be resolved with geometries postulated for the MSH plumbing system. A small shallow body approximating magma chambers directly under MSH at 0.18 Hz that is a lateral

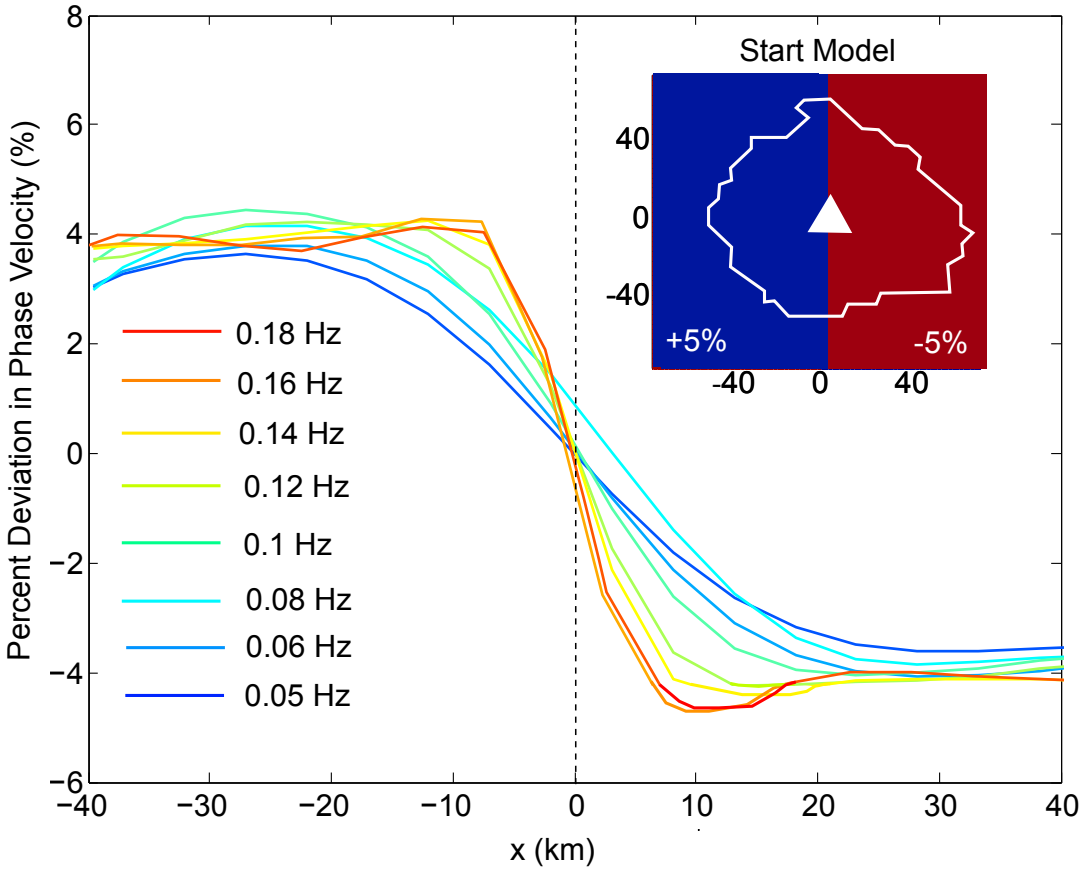

Figure 2.4: The feature recovery test of a 10% step in phase velocity across MSH, resembling Siletzia, is recovered 100% at 0.18-0.06 Hz. Inset shows model used to generate synthetic two-station phase velocity measurements. Lines show phase velocity variations along an east-west slice through the resulting inversions through the array center.

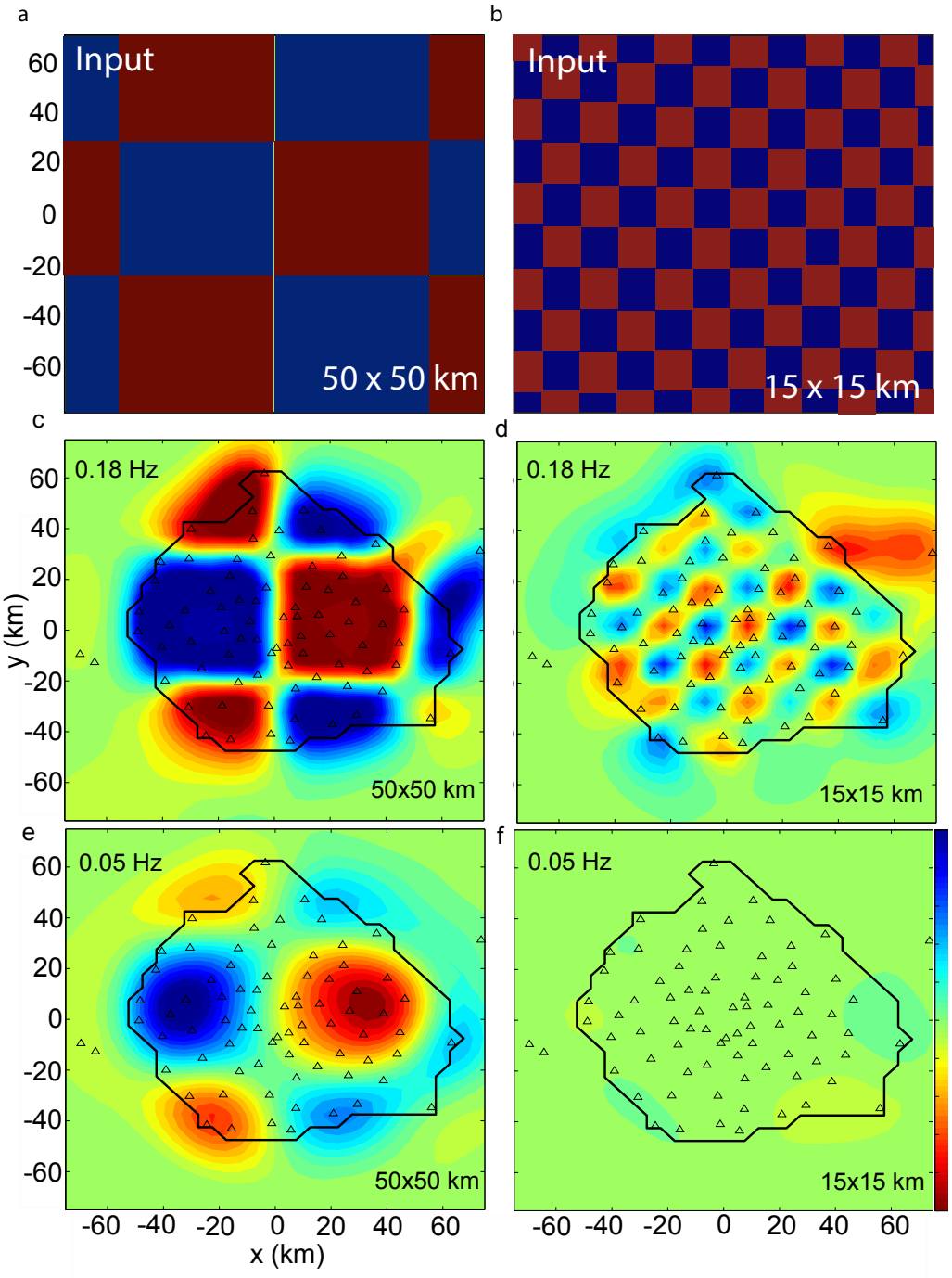

Figure 2.5: Checkerboard tests for two frequencies, 0.18 Hz and 0.05 Hz, and **a-b:** two input block sizes, 15 km and 50 km, for + 5% deviation in phase velocity**. c-d:** The output from the resolution test for 0.18 Hz and **e-f:** 0.05 Hz. The smallest resolvable box is approximately the size of half the average wavelength for each frequency. Black outline is the extent of best resolution from 0.1 Hz used to mask the shear velocity maps (**Figure 2.8**).

dimension of 5 km x 5 km or 10 km x 10 is tested (Figure A.2). First, we investigate recovery of a 10 km x 10 km 10% slow block directly beneath Mount St Helens to replicate a potential magma chamber or a partial melt zone. At 0.18Hz (a frequency with sensitivity to upper crustal structure; Figure 2.2a), the feature was recovered with 47% amplitude recovery. Conducting the same test with 5 km x 5 km block had a 19% recovery, which indicates that smaller features may be difficult to detect (Appendix A.1).

To see if deeper plumbing of MSH can be detected, a 30 km x 30 km, 10% slow block in the lower crust at 30 km depth (frequencies 0.05-0.1 Hz) was placed 20 km southeast of Mount St Helens and inverted at 0.1-0.05 Hz (Appendix A.3). This feature is meant to replicate the low velocity zone in the lower crust in Kiser et al. (2016). The feature is recovered at 40% of the maximum perturbation at 0.06 Hz. That frequency has peak sensitivity at 10-30 km depth (Figure 2.2a), so it should be possible to see such a low velocity feature with some amplitude reduction, if amplitudes are above detection, which are 0.1 km/s perturbations, equal to *Vs* uncertainty. Such a feature would be widened to 1.5 times its original size at the frequencies of 0.05 Hz (Appendix A.3).

2.5.1.3 Phase Velocity Maps

Phase velocity maps for three frequencies are presented in Figure 2.6. The sensitivity kernels (Figure 2.2a) at 0.18 Hz, 0.06 Hz, and 0.025 Hz have a maximum sensitivity of 8, 15, 45 km depth respectively, although each averages over a broad depth range. At 0.18 Hz sensitivity peaks in the upper crust, and low velocities within the well-resolved area correspond with the main volcanic arc to the east and the Chehalis basin in the northwest. Several plutons lie in high velocity zones, discussed in section 2.5.2.3. The 0.06 Hz map sampling the mid-crust shows high velocities in the west that likely delineate mafic rocks of the Siletzia terrane (section 3.3). It also shows low velocities east of MSH that correspond to widespread volcanism near the Indian Heaven volcanic field and Mount Adams (Hildreth, 2007). The transition from high to low velocities lies near the longitude of MSH, and total E-W variations in $c(\omega)$ are 8% at 15-25 km depth. The 0.025 Hz map,

based on earthquake data, shows a smoothed version of the same east-west velocity gradient as seen at 0.06 Hz. The transition from fast to slow velocity occurs approximately at MSH. These and other coherent features in phase velocity maps are discussed below with the *Vs* results.

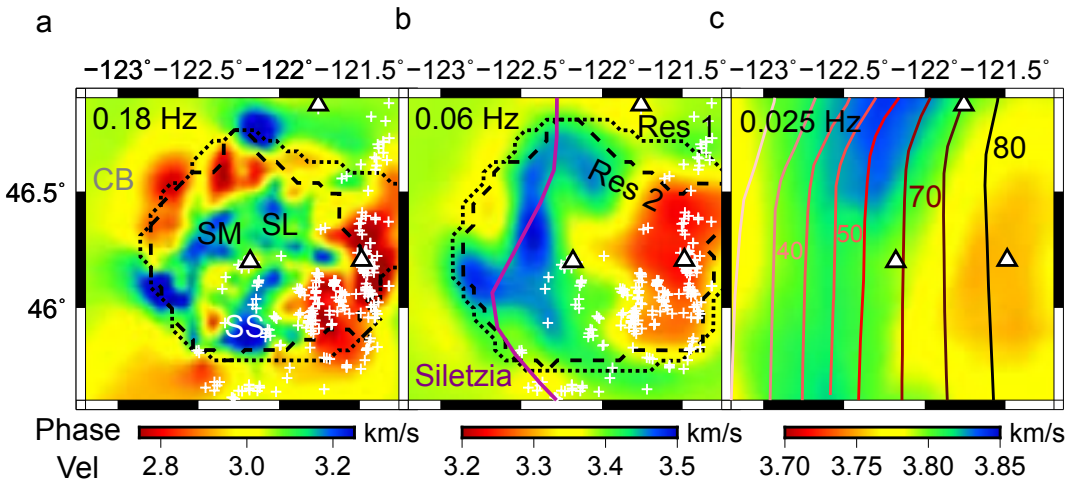

Figure 2.6: Phase velocity inversion results for three frequencies, **a:** 0.18 Hz, **b:** 0.06 Hz and **c:** 0.025 Hz. The first two are based on ambient noise the latter based on earthquakes. Maps show Quaternary vents from Hildreth (2007) (white crosses) and major volcanic edifices (white triangles). Other features geologic features of note are the Chehalis Basin (CB), Spirit Lake pluton (SL) Spud Mountain pluton (SM), and Silver Start pluton (SS) (Schuster, 2005). Depths to model slab surface shown at 0.025 Hz (dark to light red lines; McCrory et al., 2012) and at 0.06 Hz a reported east edge of Siletzia is drawn (Wells et al., 2014). Resolution contours the same as **Figure 2.3**. Note that color scale changes between panels.

2.5.2 Shear-Wave Velocity

2.5.2.1 Vs Uncertainty

Vs one-sigma uncertainties are 0.1-0.15 km/s, 0.06-0.11 km/s, and 0.8-0.12 km/s in the shallow crust (0-7.5 km depth), mid-crust (15-25 km depth), and upper mantle (45-60 km depth) respectively, based on the Monte Carlo tests described previously (section 2.2.3). Crustal velocity perturbations are 0.4 km/s and 0.3 km/s in the upper and mid-crust respectively, much larger than *Vs* uncertainties. Upper mantle variations in *Vs* are 0.2 km/s, also larger than uncertainty.

2.5.2.2 Vertical Resolution

Feature recovery tests give some indication of resolution in these inversions Figure 2.7). One set of tests investigates recovery of a low-velocity layer. Artificial phase velocities are estimated for an input *Vs* model in which a 20 km thick layer is added to a reference model, 0.5 km/s slower than surroundings, for a series of target depths. Phase velocities are perturbed by adding random noise of 0.05 km/s. The model dispersion curve is inverted in the same manner as real data with the same data weights. Three model low velocity zones have tops at 5, 15, and 37.5 km depth (Figures 2.7a-c), representing two crustal low-velocity zones and one just below the Moho. All crustal low velocity zones are recovered to full amplitude although broadened in depth. Amplitudes of the upper mantle low velocity zone is only 60% and thickened downward to twice the width. These tests indicate that a crustal feature would be easily resolvable but a feature in the upper mantle such as a mantle wedge or a subducting oceanic crust may be only partly recovered.

2.5.2.3 3D Vs Anomalies

We discuss *Vs* derived from the 1D gradient model (Figure 2.8); those from the Moho model fit the data similarly (RMS misfits of 31.7 and 31.6 m/s respectively) but show more vertically-oscillatory structure across the Moho. The *Vs* averages 3.65 $\pm$ 0.2 km/s at 10-30 km depth and 4.0-4.4 km/s in the upper mantle (40-60 km depth). *Vs* at other depth slices are in Appendix D. Previous studies similarly give *Vs* of 3.6-3.9 km/s at 10-30 km depth in the forearc (Calkins et al.,

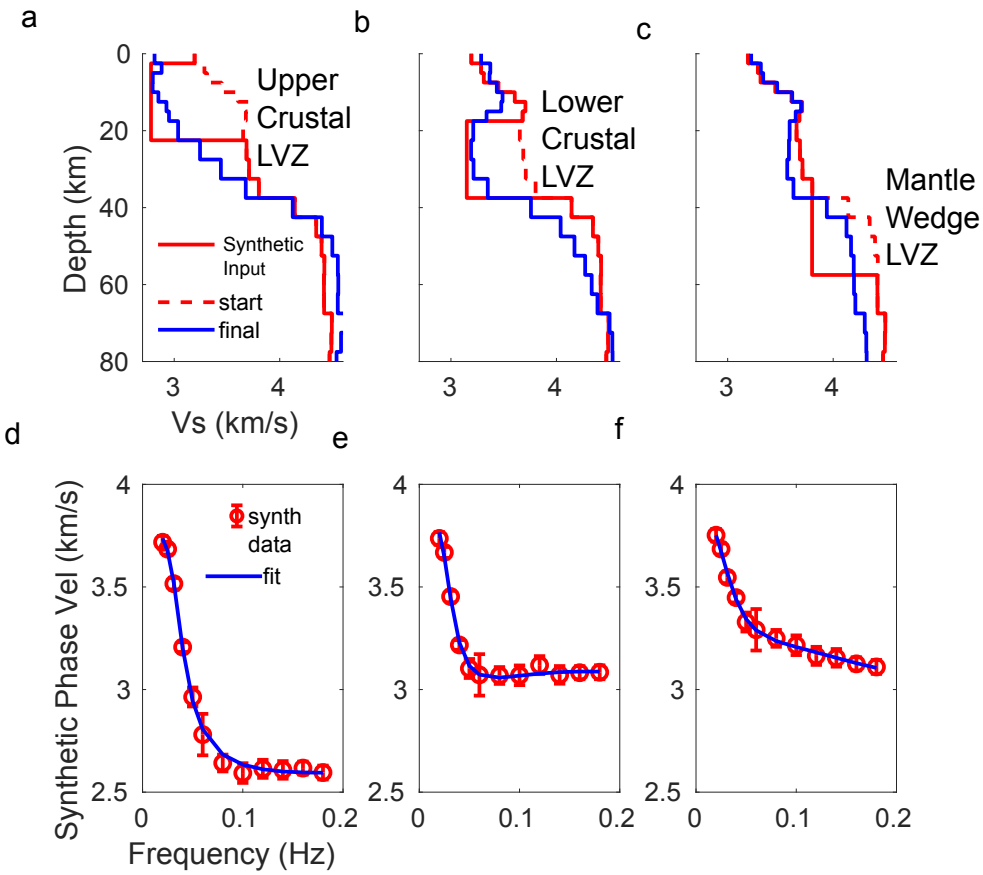

Figure 2.7: Recovery tests for inversions for *Vs* as a function of depth**. a-c:** Velocity for starting model (dashed red line, same as solid black in **Figure 2.2b**), synthetic input model (solid red line) and the resulting model from inversion (blue). In each a 20 km thick, 0.5 km/s slow low-velocity layer is added to this starting model, as described in text, with top at 5 km, 15 km, and 37.5 km for **a,b,c** respectively. **d-f:** Input model (red) and best fit (blue) dispersion curves.

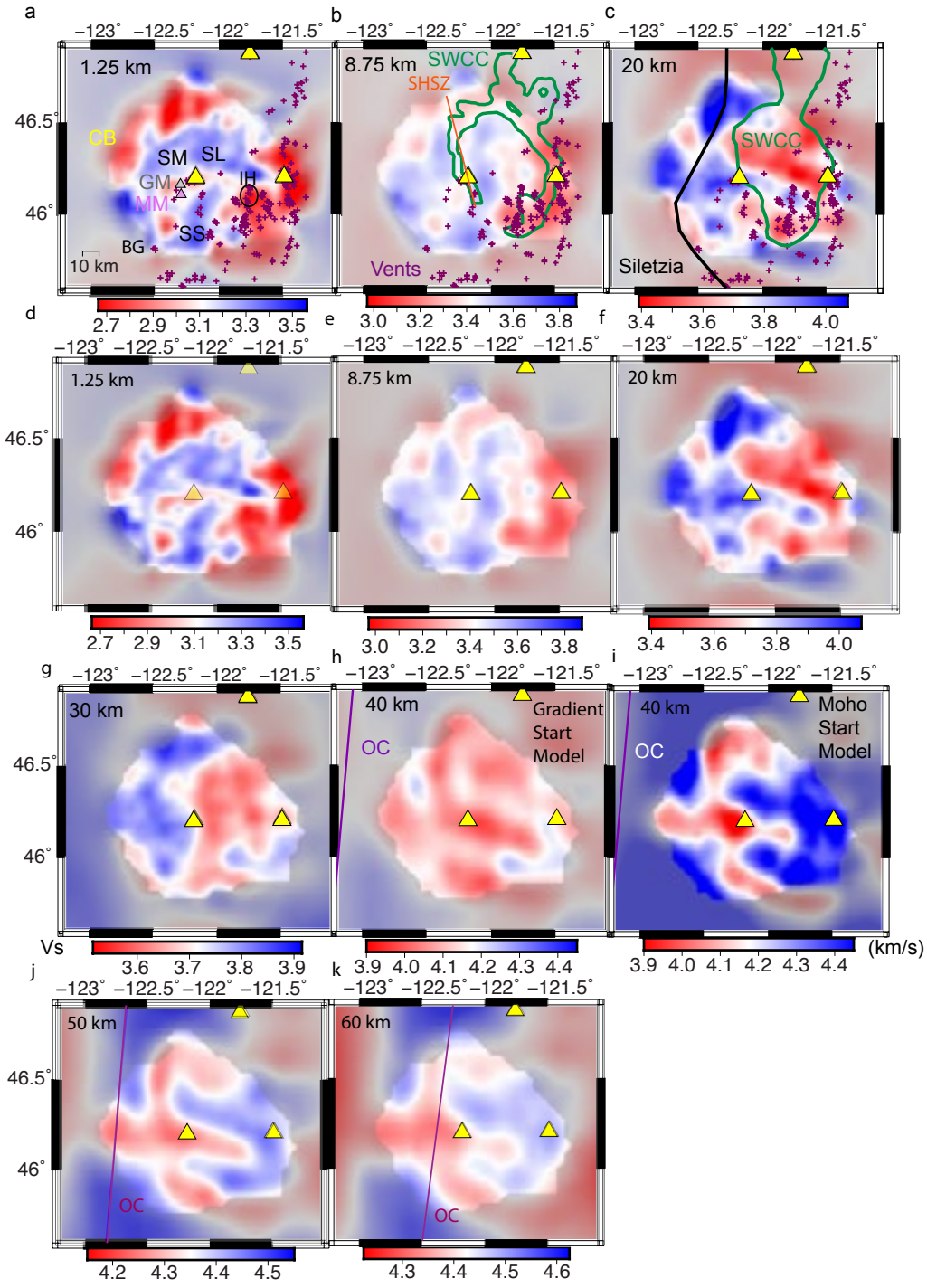
a
b
c
d
e
f
g
h
i
j
k
1.25 km
8.75 km
20 km
30 km
40 km
50 km
60 km
SWCC
SHSZ
CB
SM
SL
GM
MM
IH
SS
BG
10 km
Vents
Siletzia
OC
Gradient
Start
Model
Moho
Start
Model
Vs
(km/s)
−123˚ −122.5˚ −122˚ −121.5˚
46.5˚
46˚
2.7 2.9 3.1 3.3 3.5
3.0 3.2 3.4 3.6 3.8
3.4 3.6 3.8 4.0
3.6 3.7 3.8 3.9
3.9 4.0 4.1 4.2 4.3 4.4
4.2 4.3 4.4 4.5
4.3 4.4 4.5 4.6

Figure 2.8: Shear velocity maps for different depth slices for inversions with the gradient model. **a:** Model for upper crust (0 – 2.5 km depth) with geological features labeled: the Chehalis basin (CB), the Spirit Lake pluton (SL), the Spud Mountain pluton (SM), (BG) Battle Ground Maar, the Silver Star pluton (SS), Goat Mountain (GM) and Marble Mountain (MM); the last two are grey and pink triangles respectively (Schuster, 2005; Hildreth, 2007). **b:** Model for 7.5 – 10 km depth, showing St. Helens shear zone (SHSZ) in orange. and outlines of the Southwest Washington Crustal Conductor (SWCC) conductive bodies in green (Bedrosian et al., 2018, in green). **c:** Model at 20 km depth. The basaltic Siletzia terrane is outlined in black from magnetic anomalies (Wells et al., 1998). In **a-c:** Quaternary vents are purple crosses. **d-f:** The same as **a-c** but without the illustrated geologic features. **g**: Model for the lower crust at 30 km depth. **h:** model in the uppermost mantle at 40 km depth. **h-k**: Purple contour shows the subducting oceanic crust (OC) at this depth, from Mann et al. (subm.). **i:** Same as **h** but with a Moho model. **j:** 50 km depth, and **k:** 60 km depth.

2011). This study is compared to previous studies (Porritt et al., 2011; Gao & Shen, 2014; Shen & Ritzwoller, 2016) in Figure 2.9, which show that we have increased the resolution of the crustal imaging greatly with this method and dense array. Gao and Shen (2014) show hints of the low velocity body northeast of MSH, while others do not. None of the studies show the fast velocity west of and ending at the longitude of MSH. Mantle velocities are 4.0-4.4 km/s at 65 km depth beneath the Cascades (Gao & Shen, 2014; Shen & Ritzwoller, 2016; Wagner et al., 2010).

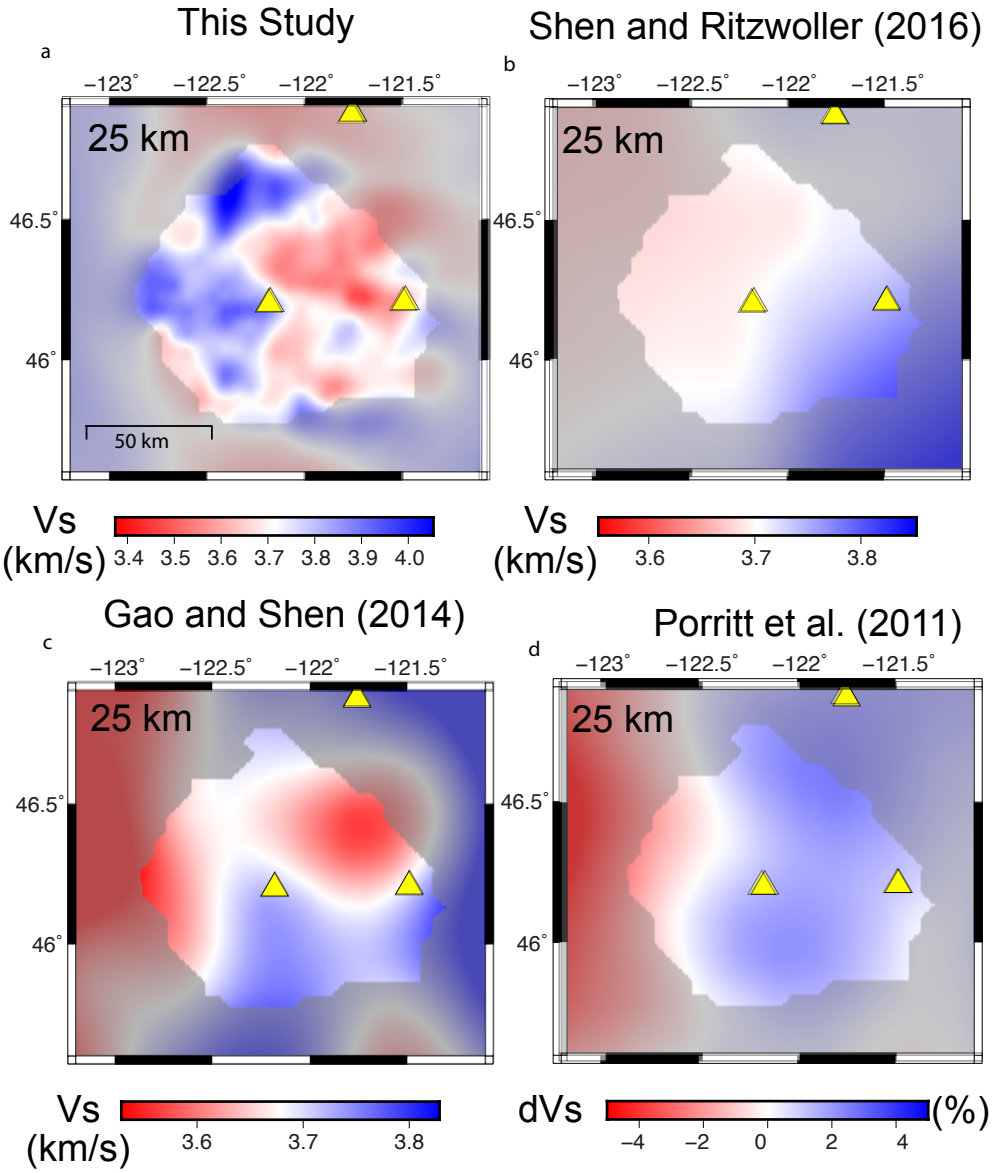

Figure 2.9: A comparison of *Vs* at 25 km **a:** from this paper and several previously-published regional models; **b:** Shen and Ritzwoller (2016). **c:** Shen and Gao (2014) **d:** Porritt et al. (2011). The triangles are the main volcanic edifices and the mask is the resolution contour from 0.1 Hz.

At shallow depths (<10 km), *Vs* variations correspond with many geologic features mapped previously (Figure 2.8a). Generally, the resolution limit at this depth is that for 0.18 Hz signals, which have a half-wavelength of 10 km. Low *Vs* at the western edge of the array (2.7 $\pm$ 0.11 km/s at 0-2.5 km depth) corresponds to the Chehalis basin (Stanley et al. 1996). High *Vs* is found NE, NW, and S of MSH where Tertiary plutons (Schuster, 2005) lie near the surface, including the Spirit Lake pluton, the Spud Mountain pluton, and the Silver Star pluton. This ring of high velocities shows *Vs* of 3.4 $\pm$ 0.15 km/s. These features are also seen in the full-waveform tomography of Flinders and Shen (2017). Farther east of Mount Saint Helens, Quaternary vents at Indian Heaven and Mount Adams lie within a region of low *Vs* of 2.7 $\pm$ 0.11 km/s. A low velocity feature extending 35 km southwest of MSH has velocities of 2.8 + 0.13 km/s. This correlates with a diffuse zone of about 30 small volcanoes that extends from Battle Ground maar to an array of basaltic vents near the Cispus River and Blue Lake (Figure 1.4; Hildreth, 2007; Swanson et al., 1989; Swanson, 1994; Evarts and Swanson, 1994). Overall there is a good correlation between surface geological features and *Vs* at >10 km depth.

In the middle to lower crust features of minimum dimension 20-30 km should be visible, given the dominant wavelengths of the signals sampling structure here. The middle to lower crust shows fast *Vs* (4.0 ± 0.10 km/s at 15 km depth decreasing to 3.85 $\pm$ 0.09 km/s at 30 km depth) west of and under MSH (Figure 2.10c,e; Figures 2.8c-d). Global averages for *Vs* on continents are 3.4-3.7 km/s for these depths, combining *Vp* compilations (Christensen & Mooney, 1995) with common *Vs*-*Vp* relationships (Brocher, 2005). Within the contiguous United States, mid-crustal *Vs* from ambient-noise inversions are slightly faster, commonly 3.5-3.8 km/s (Shen & Ritzwoller, 2016). Near Mount Rainier, Obrebski et al. (2015) shows lower crustal *Vs* of 3.6-3.85 km/s, while Flinders and Shen (2017) show *Vs* of 3.7-3.9 km/s at the longitude of MSH, at similar depths. Our observations are comparable to, if slightly faster, perhaps a result of the high resolution from the iMUSH array.

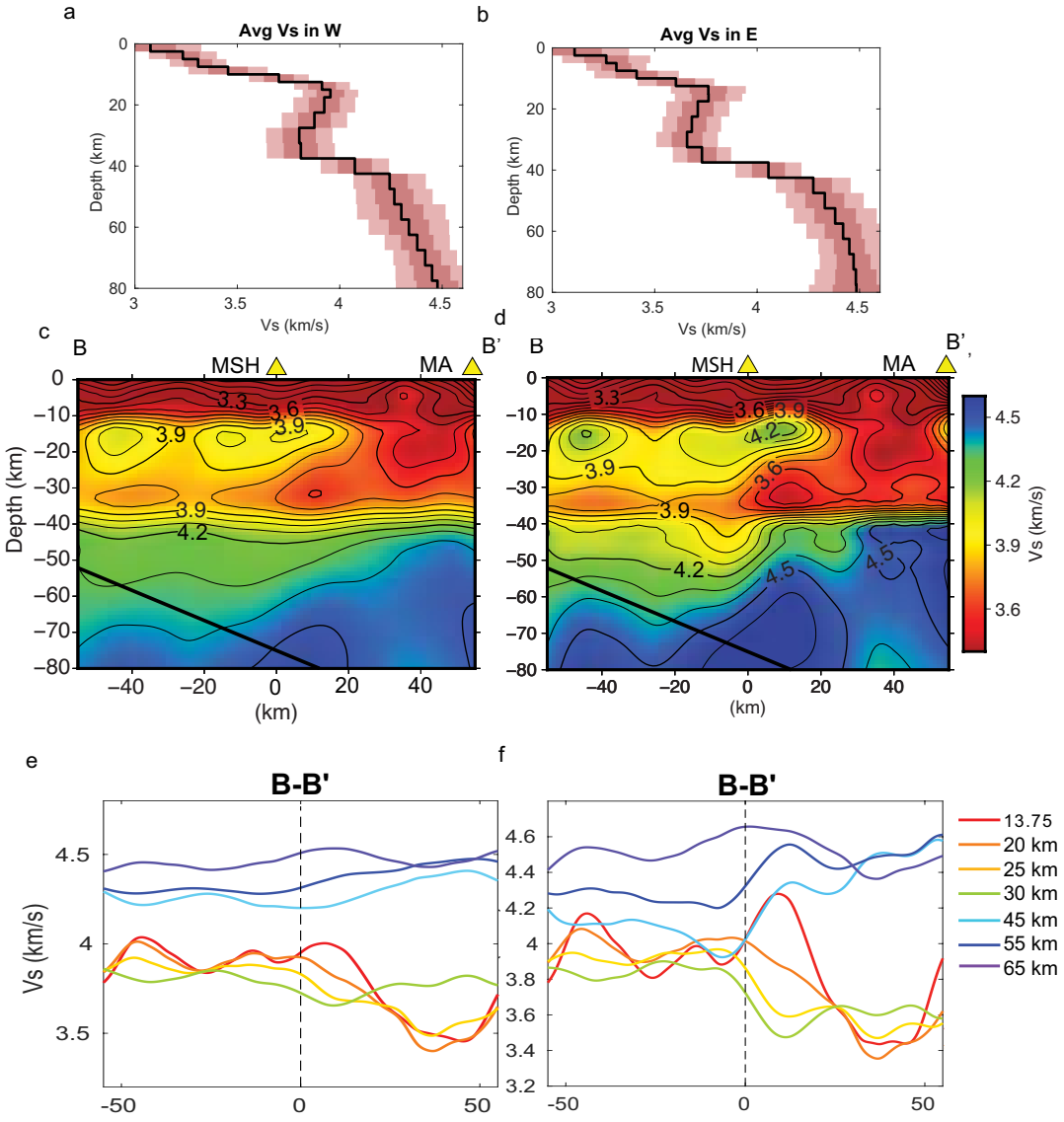

Figure 2.10: East-west transect through MA and MSH (line B-B') (transect lines shown in **Figure 2.11b**). **a:** Average *Vs* variation with depth n the west/forearc; see **Figure 1.3b** for region averaged. **b:** same for the eastern, volcanic average. 1D *Vs* models show 1 and 2-sigma uncertainty from Monte Carlo as shading. **c:** E-W *Vs* transect through the gradient model B-B'. Black line shows oceanic Moho from Mann et al. (subm). **d:** same for model with free Moho**. e-f:** *Vs* at different depths along the same E-W transect for gradient and Moho model respectively.

Slower *Vs* (3.5-3.65 km/s) is imaged at 15-30 km depths in a 50 km wide region between MSH, Mount Rainier, and Mount Adams (Figure 2.8c). The distribution of this feature is similar to a combination of the Southern Washington Cascades Conductor (SWCC) (Bedrosian et al., 2018; Hill et al., 2009; Stanley et al., 1987) and the Quaternary vent field (Hildreth, 2007), particularly in the Indian Heaven volcanic field. Low P-wave velocities here are also seen in active-source imaging (Kiser et al., 2016). Given this geometry, it seems likely that these low velocities are related to Quaternary volcanism (Bedrosian et al., 2018).

In the uppermost mantle (Figure 2.8e-f), *Vs* is somewhat dependent on choice of starting model and smoothness condition on the Moho (compared in Figure 2.8e-f; Figure 2.10; Figure 2.11; and Appendix D), reflecting a decrease in resolution and sensitivity with increasing depth. The upper mantle velocities are between 4.2 km/s and 4.4 km/s, with lower velocities beneath the west half of the array. The higher values resemble typical upper mantle globally (Dziewonski & Anderson, 1982; Christensen & Mooney, 1995) and regionally (Shen & Ritzwoller, 2016). Joint inversions below Mount Rainier (Obrebski et al., 2015) give 4.15-4.35 km/s. The low uppermost-mantle velocities are seen west of MSH and conspire with high velocities in the lower crust to make the Moho much weaker as a discontinuity in that region, similar to receiver function and active source results (e.g., Mann et al., 2017; subm.; Hansen et al., 2016). For inversions using the Moho model, the Moho step increases from 3.7 km/s to 4.2 km/s (0.5 km/s) within 10 km of the Moho in the west and from 3.6 km/ to 4.4 km/s (0.8 km/s) in the east. When the gradient model is used, *Vs* only changes from 3.9 km/s to 4.2 km/s (0.3 km/s) within 10 km of the Moho in the west and from 3.6 km/s to 4.3 km/s (0.7 km/s) in the east. These data do not have sensitivity to image structure within the deeper subducting plate.

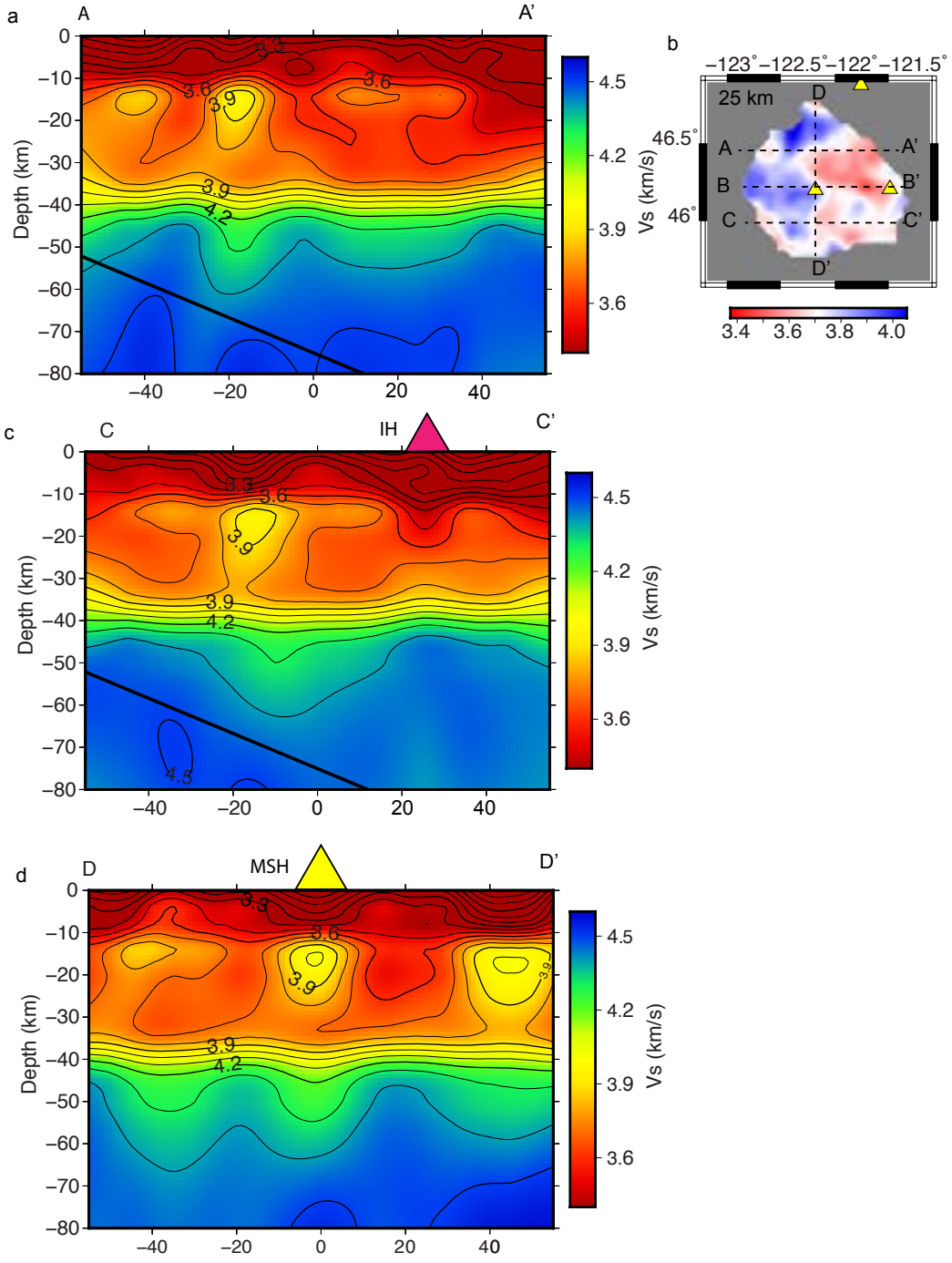

Figure 2.11: Comparison of three transects with a gradient model. Locations of transects shown in **b**. **a:** A-A' transect 25 km north of MSH. **c:** This C-C' cross section goes through Indian Heaven (IH), 25 km south of MSH. **d:** This D-D' cross section runs north-south through MSH.

3 Discussion

3.1 Upper crust

At 0-8 km depth, features in the seismic tomography images largely reflect near-surface geology. The distribution of the local plutons and sedimentary basins (Figure 2.8a) correlate well with high and low velocity features respectively, and agree well with prior studies (Flinders & Shen, 2017; Schuster 2005). These same plutons and sedimentary basins are visible in local-earthquake tomography (Ulberg et al., in prep.). They also see a low velocity zone along the St. Helens Shear Zone (SHSZ) northwest of MSH, which is weakly imaged in the current results (Figure 2.8b), with lower amplitude (-3% *dVs* compared to -5% dVp in Ulberg et al., in prep.). A low *Vs* feature (3.0 $\pm$ 0.13 km/s) extending southwest from MSH aligns with extinct volcanic centers at Goat Mt. and Marble Mt (Figure 2.8a, grey and pink triangles respectively) following a trend of other Quaternary vents (Hildreth, 2007). Lees and Crosson (1989) image a similar low-velocity feature near MSH, but our well-resolved feature extends further south and suggests a larger, continuous feature perhaps extending to the Battle Ground maar (BG). The southeast part of the low-velocity feature corresponds well to the Indian Heaven – Mount Adams region of abundant Quaternary vents. Although these vents are largely basaltic (Hildreth, 2007), their *Vs* is low in the upper crust and likely reflects the altered and porous nature of the volcanic cover.

3.2 Absence of Moho beneath the forearc

The Moho discontinuity to the east of MSH disappears within a few km west of the summit, in Pn amplitudes (Brocher et al., 2003), PmP reflections (Hansen et al., 2016), and receiver functions (Mann et al., subm.). The surface-wave tomography presented here similarly shows steeper velocity gradients across the Moho to the east than west, although the amplitude of the anomaly is sensitive to initial model at this depth (Figure 2.10; Appendix D). With the gradient model, the *Vs* step across the Moho in the west is $\leq$ 0.3 km/s compared with 0.85 km/s in the east, whereas with the Moho model the *Vs* step in the west is 0.1 km/s compared with 0.9 km/s in the east, which is measured as the *Vs* change between 25 and 45 km depth. The weak-to-absent

forearc Moho is a robust feature in these current results, interpreted here as both a high *Vs* in the lower-crust and a low uppermost-mantle *Vs*. The Moho is reduced in large part due to high crustal velocity and is only weakly a mantle effect.

Previous studies (e.g., Brocher et al., 2003; Bostock et al., 2002; Hansen et al., 2016), explain the Moho reduction to be entirely due to a slow, hydrated, serpentinized forearc mantle wedge. These studies are only constraining velocity contrasts rather than absolute velocities, so they would not be able to attribute the velocity contrast to the crustal velocities as in this study. A fully hydrated forearc mantle wedge would have *Vs* ~ 4.0-4.1 km/s (Abers et al., 2017), with antigorite-serpentine and chlorite the main hydrous phases affecting *Vs*. These predictions are similar to *Vs* imaged there (Figure 2.10; Figure 2.11), although slightly faster perhaps due to low resolution of the 0.04-0.06 Hz phase velocities that control *Vs* at these depths. A hydrated forearc mantle wedge agrees with the *Vs* in the upper mantle, however the crustal velocities contribute to the Moho reduction equally.

The Moho velocity contrasts are reduced west of MSH both because of the presence of the high-*Vs* lower crust (3.95 ± 0.1 km/s) and a hydrated uppermost mantle (4.0-4.1 km/s) (e.g., Hansen et al., 2016; Bostock et al., 2002) (Figure 2.8). Overall the Moho velocity contrast vanishes at least equally due to the presence of high-*Vs* crust in the forearc, as mantle wedge hydration alone (Hyndman and Peacock, 2003) is insufficient to produce this observation.

3.3 Lower crust in the forearc: Siletzia?

The fast middle-lower crust in the west of the study area abruptly ends at the longitude of MSH (Figure 2.8c), and has *Vs* of 3.95 $\pm$ 0.1 km/s at 20-30 km depth. The distribution and seismic properties of the fast middle-lower crust correspond to the magnetically imaged eastward extent of the Siletzia terrane, a largely gabbroic Eocene-Paleocene accreted large igneous province (Wells et al., 2014). Magnetic field anomalies indicate a slightly farther west downdip end to Siletzia than the eastern extent imaged in this study (Wells et al., 2014), although it has been suggested that MSH is localized by the eastern Siletz limit (Parsons et al., 1998). By contrast, regional mantle

imaging have suggested that Siletzia extends hundreds of km further east of MSH (Schmandt & Humphreys, 2011); if so then we infer the imaging involves only the mantle lithosphere and not Siletz crust. Previous imaging, including with ambient noise from regional arrays, was not able to resolve the fast crustal region of the North American crust (Figure 2.9).

To quantify the extent to which temperature rather than composition could explain the lateral velocity variations of the lower crust, we calculate a range of temperatures consistent with surface heat flow (Pollack et al., 1993; Blackwell et al., 1990) and compare them with predictions of *Vs* variations with temperature for Siletz gabbros. Geotherms in the forearc are calculated using heat flow from the data set of Pollack et al. (1993), averaged from point measurements in the forearc box shown on Figure 1.3. These measurements are in the range 27 - 47 mW/m^2 (Figure 1.3). To calculate temperature at mid-crustal depths these heat flow values are combined with an assumed thermal conductivity of 2.5 – 3.5 $Wm^{-1}K^{-1}$ (Till et al., in review) and extrapolated linearly, as expected for a region in steady state and with negligible heat production such as the Siletz gabbros. These temperatures are then used to calculate *Vs* at depth in the forearc from petrologic models (Figure 3.1b), as described in Till et al. (in review). Specifically, we estimate modal mineralogies from major element oxide compositions for a suite of 16 samples of the Crescent-Siletz basalt (Phillips et al., 2017; Sisson et al., 2014), using the PerpleX free-energy minimization algorithm (Connolly, 2005). Solution models and other parameters are described in Abers et al. (2016); calculations are otherwise similar to those described in Obrebski et al. (2015). From these compositions we calculate *Vs* as a function of pressure and temperature following Abers and Hacker (2016); see Figure 1.15a. For the range of plausible forearc geotherms, *Vs* is predicted to be 3.85 $\pm$ 0.05 km/s at 20 km depth and 4.00 $\pm$ 0.10 km/s at 30 km/s (Figure 1.15b). This agrees within uncertainty with the observed *Vs* in the west, at depths less than 30 km. At depths between 30 km and the Moho, the observed *Vs* is systematically less than the predicted Siletz *Vs*, but the discrepancy is small. The *Vs* is consistent with the composition of the *Vs* of the Siletzia terrane and the temperatures inferred from heat flow, so it seems likely that Siletzia makes up the basement west of MSH. These high velocities end abruptly at MSH and are not imaged farther east. Hence,

the Siletzia terrane likely ends at MSH, and models (Parsons et al., 1998) that explain the precise location of MSH as a consequence of the edge of Siletzia are plausible (Parsons et al., 1998). The Siletzia terrane may act as a westward barrier to magma, localizing volcanism at MSH.

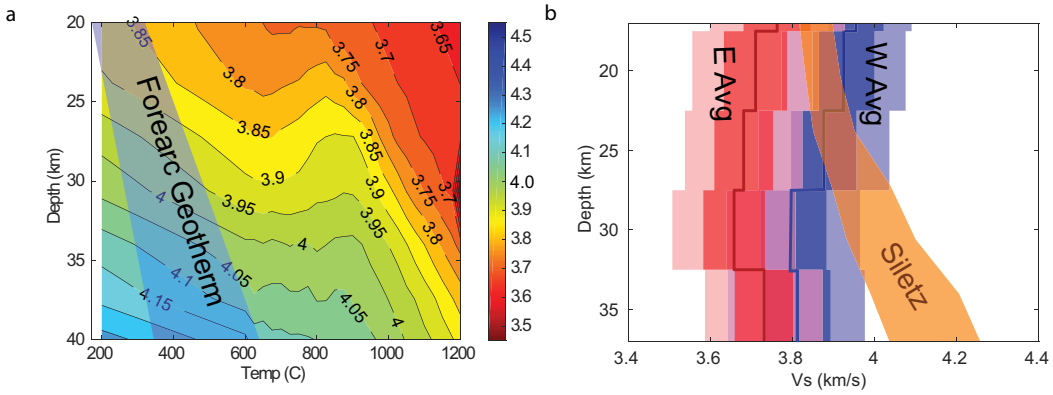

Figure 3.1: a: Estimates of *Vs* averaged for samples of Siletz-Crescent basalts, calculated at varying temperature and depth, along with the allowed range of forearc temperatures, as described in text. **b:** Comparison of this predicted *Vs* versus depth for Siletzia within the forearc geotherms, with average observed *Vs* east and west of MSH (area in black boxes **Figure 1.3b**).

3.4 Melt Bodies and Melt Pathways Between Arc Volcanoes

Recent studies have suggested that there is a lower crustal partial melt zone that for some MSH lavas. Blatter et al. (2017) concludes experimentally that the Yn dacite, typical of MSH eruptions, is possibly sourced from the lower crust (depth of 25-30km) at temperatures ≥925°C. Kiser et al. (2016) image a low *Vp* anomaly at 30 km depth, 20 km southeast of MSH, that they interpret as a partial melt zone crustal velocities east of MSH on two 2D profiles. However their lowest velocities, 6.5 km/s at 30 km depth, have alternative explanations. Bedrosian et al. (2018) image a mid-crustal (20 km) conductive feature between MSH, Mount Adams, and Mount Rainier, which they interpret as partial melt and associate with the southern Washington Cascades conductor (SWCC; Stanley et al., 1987). In map view (Figure 2.8c) the crust has significantly lower *Vs* east of MSH than west of it (3.45-3.7 km/s at 15-25 km depth), and the low-*Vs* region imaged in this study is similar in shape to the mid-crustal SWCC (Bedrosian et al., 2018). The low-*Vs* region

is localized between 15-25 km, 35 km east of MSH, towards Mount Adams. The lower crust *Vs* is also low where Kiser et al. (2016) images a low-velocity zone, 3D images indicate that the low velocity zone is more extensive than a localized feature southeast of MSH. While it is clear that there are conductive and low velocity features in the lower crust near MSH, offset towards the arc, it is debated if there are broad regions of partial melt.

It is unclear if this low-Vs body is due to melt or composition, so first, we attempt to explain these low velocities with composition and temperature to see if melt is required. Obrebski et al. (2015) show *Vs* for a range of compositions at 550 C and 0.8 GPa, derived from the database of Jagoutz and Behn (2013). These velocities are near 3.8 ± 0.1 km/s for a wide range of intermediate-to-felsic compositions, and always over 3.7 km/s. To estimate *Vs* at higher temperatures, we use derivatives of *Vs* with temperature (Till et al., in review), which are -0.7 m/s/K for mafic Siletz gabbros. Increasing the temperature to 850° C would decrease *Vs* by 0.2 km/s to 3.6 ± 0.1 km/s, if the Vs derivative is valid for more felsic rocks. However, direct calculations on more felsic rocks do not produce such low *Vs* (e.g., Abers et al., 2016; Brownlee et al., 2011), constant-composition *dVs/dT* derivatives are half to a third this value calculated for equilibrium petrology (e.g., Christensen and Mooney, 1995; Christensen, 1996), and similar Perple_X-based calculations on felsic rocks do not show *Vs* < 3.6 km/s. Thus, the low velocities seen between Mount Adams and MSH are difficult to explain with composition alone.

It is likely that the velocities may reflect a small percent of partial melt, since melt (or other pore fluids) have a strong effect on *Vs* (McCarthey & Takei, 2011). Analyzing the percentage partial melt present is beyond the scope of this paper, because melt effects on *Vs* in felsic rocks are complex, the starting composition is poorly known, and other factors such as water content of the melt may have strong effects on *Vs*. Bedrosian et al. (2018) concludes that the lower crustal conductive feature is explained by 3-10% interconnected dacitic melt, and that a water-only model is unlikely given petrologic studies (Blatter et al., 2017; Cashman et al., 2017; Claiborne et al., 2010). The location of the low-*Vs* and high conductivity feature is associated with abundant diffuse Quaternary volcanism, and may feed numerous vents between MSH and Mount Adams. The

lower crustal low-*Vs* zone and conductive feature are not obviously connected to the upper magma chamber of MSH or MA, suggesting that only during episodic recharge is the lower crustal partial melt source connected to the eruptive chamber (Bedrosian et al., 2018). However, connections may exist that are just below the resolution level of the study. This study constrains that there likely exists a partial melt body that is small, but large enough that it is above the resolution limit.

3.5 Conclusions

The main conclusions of this study are the following:

1. Ambient noise tomography works effectively for relatively small, dense arrays like iMUSH at depths shallower than 50-60 km. Image recovery is limited by the wavelengths of the relevant signals, not station spacing in this geometry.
2. The observed absence of Moho reflectivity above the forearc mantle is consistent with *Vs* images from this study, which constrains absolute velocities. The Moho vanishes both because of the high-velocity Siletz crust above the forearc mantle (3.95 $\pm$ 0.1 km/s) and the low-velocity, hydrated mantle wedge, which has a similar *Vs* near 4.0 km/s. An understanding of upper plate geology is necessary in order to interpret hydration from Moho properties.
3. The Siletzia terrane makes up the middle and lower crust everywhere west of MSH, where it abruptly ends. Its coincident boundary with MSH and the region of low forearc heat flow could be an explanation for the specific location of the volcanic edifice; the terrane may act as a westward barrier for volcanism. However, it is still unclear why volcanism occurs here over such a shallow subducting plate.
4. The *Vs* between the main volcanoes (MSH, Mount Rainier, Indian Heaven, and Mount Adams) may require partial melt, at least at mid-crustal depths. MSH likely has a melt source where temperatures are hotter near the arc.

REFERENCE

Abers, G. A., Eilon, Z., Gaherty, J. B., Jin, G., Kim, Y. H., Obrebski, M., & Dieck, C. (2016). Southeast Papuan crustal tectonics: Imaging extension and buoyancy of an active rift. *Journal of Geophysical Research: Solid Earth*, *121*(2), 951-971.

Abers, G. A., van Keken, P. E., & Hacker, B. R. (2017). The cold and relatively dry nature of mantle forearcs in subduction zones. *Nature Geoscience*, (April). https://doi.org/10.1038/ngeo2922

Abers, G. A., & Hacker, B. R. (2016). A MATLAB toolbox and Excel workbook for calculating the densities, seismic wave speeds, and major element composition of minerals and rocks at pressure and temperature. *Geochemistry, Geophysics, Geosystems*, *17*(2), 616-624.

Abers, G.A., unpub. software manual, 2018

Aki, K. (1957). Space and time spectra of stationary stochastic waves, with special reference to microtremors. *Bull. Earthq. Res. Inst.*, *35*, 415-456.

Allen, J.E., 1975, Volcanoes of the Portland area, Oregon: Oregon Department of Geology and Mineral Industries, The Ore Bin, v. 37, no. 9, p. 145-157.

Annen, C., Blundy, J. D., Sparks, R. S. J., & Gene, D. E. (2006). The Genesis of Intermediate and Silicic Magmas in Deep Crustal Hot Zones, *47*(3), 505–539. https://doi.org/10.1093/petrology/egi084

Ardhuin, F., Stutzmann, E., Schimmel, M., & Mangeney, A. (2011). Ocean wave sources of seismic noise. *Journal of Geophysical Research: Oceans*, *116*(9), 1–21. https://doi.org/10.1029/2011JC006952

Bedrosian, P.A., Peacock, J.R., Bowles-Martinez, E., Schultz, A. and Hill, G.J., 2018. Crustal inheritance and a top-down control on arc magmatism at Mount St. Helens. *Nature Geoscience*.

Behn, M. D., & Kelemen, P. B. (2006). Stability of arc lower crust: Insights from the Talkeetna arc section, south central Alaska, and the seismic structure of modern arcs. *Journal of Geo-*

physical Research: Solid Earth, *111*(11), 1–20. https://doi.org/10.1029/2006JB004327

Bensen, G. D., Ritzwoller, M. H., Barmin, M. P., Levshin, A. L., Lin, F., Moschetti, M. P., … Yang, Y. (2007). Processing seismic ambient noise data to obtain reliable broad-band surface wave dispersion measurements. *Geophysical Journal International*, *169*(3), 1239–1260. https://doi.org/10.1111/j.1365-246X.2007.03374.x

Blackwell, D. D., Steele, J. L., Kelley, S., & Korosec, M. A. (1990). Heat flow in the state of Washington and thermal conditions in the Cascade Range. *Journal of Geophysical Research*, *95*(B12), 19,419-495,516.

Blakely, R. J., Brocher, T. M. &Wells, R. E. Subduction-zone magnetic anomalies and implications for hydrated forearc mantle. Geology 33, 445–448 (2005). 16.

Blatter, D. L., Sisson, T. W., & Hankins, · W Ben. (2017). *Voluminous arc dacites as amphibole reaction-boundary liquids*. *Contrib Mineral Petrol* (Vol. 1). Springer Berlin Heidelberg. https://doi.org/10.1007/s00410-017-1340-6

Bostock, M. G., Hyndman, R. D., Rondenay, S., & Peacock, S. M. (2002). An inverted continental Moho and serpentinization of the forearc mantle. *Nature*, *417*(6888), 536.

Brocher, T. M. (2005). Empirical Relations between Elastic Wavespeeds and Density in the Earth ' s Crust, *95*(6), 2081–2092. https://doi.org/10.1785/0120050077

Brocher, T. M., Parsons, T., Trehu, A. M., Snelson, C. M., & Fisher, M. A. (2003). Seismic evidence for widespread serpentinized forearc upper mantle along the Cascandia margin. *Geology*, *31*(3), 267–270. https://doi.org/10.1130/0091-7613(2003)031<0267:SEFWSF>2.0.CO;2

Brownlee, S. J., Hacker, B. R., Salisbury, M., Seward, G., Little, T. A., Baldwin, S. L., & Abers, G. A. (2011). Predicted velocity and density structure of the exhuming Papua New Guinea ultrahigh-pressure terrane. *Journal of Geophysical Research: Solid Earth*, *116*(B8).

Buckovic, W.A., 1979, The Eocene deltaic system of west- central Washington, in Armentrout, J.M., Cole, M.R., and TerBest, H., eds., Cenozoic Paleogeography of the Western United States: Society of Economic Paleon- tologists and Mineralogists, Pacifi c Coast Paleogeography Symposium 3, p. 147–163.

Calkins, J. A., Abers, G. A., Ekstrm, G., Creager, K. C., & Rondenay, S. (2011). Shallow structure of the Cascadia subduction zone beneath western Washington from spectral ambient noise correlation. *Journal of Geophysical Research: Solid Earth*, *116*(7), 1–20. https://doi.org/10.1029/2010JB007657

Cashman, K. V., Sparks, R. S. J., & Blundy, J. D. (2017). Vertically extensive and unstable magmatic systems: a unified view of igneous processes. *Science*, *355*(6331), eaag3055.

Christensen, N. I. (1995). Seismic velocity structure and composition of the continental crust : A global view, *100*, 9761–9788.

Christensen, N. I., & Mooney, W. D. (1995). Seismic velocity structure and composition of the continental crust: A global view. *Journal of Geophysical Research: Solid Earth*, *100*(B6), 9761-9788.

Claiborne, L. L., Miller, C. F., & Wooden, J. L. (2010). Trace element composition of igneous zircon: a thermal and compositional record of the accumulation and evolution of a large silicic batholith, Spirit Mountain, Nevada. *Contributions to Mineralogy and Petrology*, *160*(4), 511-531.

Clayton, G., 1980, Geology of White Pass—Tumac Mountain area, Washington: Washington Division of Geology and Earth Resources Open-File Report 80-8, scale 1:24,000.

Clynne, M.A., Ramsey, D.W., and Wolfe, E.W., 2005, Pre- 1980 eruptive history of Mount St. Helens, Washington: U.S. Geological Survey Fact Sheet 2005-3045, p.4

Coney, P. J., Jones, D. L., & Monger, J. W. (1980). Cordilleran suspect terranes. *Nature*, *288*(5789), p. 329

Connolly, J. A. (2005). Computation of phase equilibria by linear programming: a tool for geodynamic modeling and its application to subduction zone decarbonation. *Earth and Planetary Science Letters*, *236*(1-2), p. 524-541

Conrey, R.M., Uto, K., Uchiumi, S., Beeson, M.H., Madin, I.P., Tolan, T.L., and Swanson, D.A., 1996, Potassium-Ar- gon ages of Boring Lava, northwest Oregon and southwest Washington: Isochron/West, no. 63, p. 3-9.

Crandell, D.R., 1987, Deposits of pre-1980 pyroclastic flows and lahars from Mount St. Helens volcano, Washington: U.S. Geological Survey Professional Paper 1444, p. 91

Delph, J. R., Ward, K. M., Zandt, G., Ducea, M. N., & Beck, S. L. (2017). Imaging a magma plumbing system from MASH zone to magma reservoir. *Earth and Planetary Science Letters*, *457*, p. 313-324.

De Siena, L., Thomas, C., Waite, G. P., Moran, S. C., & Klemme, S. (2014). Attenuation and scattering tomography of the deep plumbing system of Mount St. Helens. *Journal of Geophysical Research: Solid Earth*, *119*(11), p. 8223-8238.

Duncan, R.A., 1982, A captured island chain in the coast range of Oregon and Washington: Journal of Geophysi- cal Research, v. 87, p. 10,827–10,837, doi: 10.1029 /JB087iB13p10827.

Dziewonski, A. M., & Anderson, D. L. (1984). Seismic Tomography of the Earth's Interior: The first three-dimenstional models of the earth's structure promise to answer some basic questions of geodynamics and signify a revolution in earth science. *American Scientist*, *72*(5), 483-494.

Ekström, G., Abers, G. A., & Webb, S. C. (2009). Determination of surface-wave phase velocities across USArray from noise and Aki's spectral formulation. *Geophysical Research Letters*, *36*(18), p. 5–9. https://doi.org/10.1029/2009GL039131

Evarts, R.C., and Swanson, D.A., 1994, Geologic transect across the Tertiary Cascade Range, southern Washington, ch. 2H in D.A. Swanson and R.A. Haugerud, eds., Geologic field trips in the Pacific Northwest: Dept. of Geological Sciences, University of Washington, in conjunction with 1994 Annual Meeting of the Geological Society of America, Seattle, v. 2, p. 2H-1-31.

Flinders, A. F., & Shen, Y. (2017). Seismic evidence for a possible deep crustal hot zone beneath Southwest Washington. *Scientific Reports*, (June), p. 1–10. https://doi.org/10.1038/s41598-017-07123-w

Gao, H., & Shen, Y. (2014). Upper mantle structure of the Cascades from full-wave ambient noise tomography: Evidence for 3D mantle upwelling in the back-arc. *Earth and Planetary*

Science Letters, *390*, p. 222-233.

Gerstoft, P., Fehler, M. C., & Sabra, K. G. (2006). When Katrina hit California. *Geophysical Research Letters*, *33*(17), p. 2–7. https://doi.org/10.1029/2006GL027270

Hammond, P. E., & Korosec, M. A. (1983). Geochemical analyses, age dates, and flow-volume estimages for quaternary volcanic rocks, Southern Cascade Mountains, Washington. *Portland State Univ., OR (USA). Dept. of Earth Sciences; Washington Div. of Geology and Earth Resources, Olympia (USA)*.

Hansen, S. M., Schmandt, B., Levander, A., Kiser, E., Vidale, J. E., Abers, G. A., & Creager, K. C. (2016). Seismic evidence for a cold serpentinized mantle wedge beneath Mount St Helens. *Nature Communications*, *7*, p. 13242. https://doi.org/10.1038/ncomms13242

Harmon, N., Gerstoft, P., Rychert, C. A., Abers, G. A., de la Cruz, M. S., & Fischer, K. M. (2008). Phase velocities from seismic noise using beamforming and cross correlation in Costa Rica and Nicaragua. *Geophysical Research Letters*, *35*(19), p. 1–6. https://doi.org/10.1029/2008GL035387

Heller, P.L., Peterman, Z.E., O'Neil, J.R., and Shafi qullah, M., 1985, Isotopic provenance of sandstones from the Eocene Tyee Formation, Oregon Coast Range: Geologi- cal Society of America Bulletin, v. 96, p. 770–780, doi: 10.1130 /0016 -7606 (1985)96 <770: IPOSFT>2.0 .CO;2.

Herrmann, R. B., & Ammon, C. J. (2004). Surface Waves, Receiver Functions and Crustal Structure. Computer Programs in Seismology, Version 3.30. Saint Louis University.

Hildreth, W. (2007). Quaternary magmatism in the Cascades; geologic perspectives. *U.S. Geological Survey Professional Paper 1744*, p. 125. Retrieved from http://www.google.com/search?client=safari&rls=en-us&q=Quaternary+magmatism+in+the+Cascades%5Cn+geologic+perspectives&ie=UTF-8&oe=UTF-8%5Cnpapers2://publication/uuid/76F4FA23-CC0C-438E-9BFD-4952CAB6233B

Hill, G. J., Caldwell, T. G., Heise, W., Chertkoff, D. G., Bibby, H. M., Burgess, M. K., … Cas, R. A. F. (2009). Distribution of melt beneath Mount St Helens and Mount Adams inferred from

magnetotelluric data. *Nature Geoscience*, *2*(11), p. 785–789. https://doi.org/10.1038/ngeo661

Hoblitt, R. P., Crandell, D. R., & Mullineaux, D. R. (1980). Mount St. Helens eruptive behavior during the past 1,500 yr. *Geology*, *8*(11), p. 555-559.

Hyndman, R. D., & Peacock, S. M. (2003). Serpentinization of the forearc mantle. *Earth and Planetary Science Letters*, *212*(3-4), p. 417-432.

Hyndman, R. D., & Wang, K. (1993). Thermal Constraints on the Zone of Major Thrust Earthquake Failure ' Zone earthquakes that compared the Caseadia subduction across the Cascadia margin the Cascadia margin , J ,. *Journal of Geophysical Research*, *98*, p. 2039–2060.

Inoue, H., Fukao, Y., Tanabe, K., & Ogata, Y. (1990). Whole mantle P-wave travel time tomography. *Physics of the Earth and Planetary Interiors*, *59*(4), p. 294–328. https://doi.org/10.1016/0031-9201(90)90236-Q

Jagoutz, O., & Behn, M. D. (2013). Foundering of lower island-arc crust as an explanation for the origin of the continental Moho. *Nature*, *504*(7478), p. 131.

Janiszewski, H. A. (2018). *New Insights on the Structure of the Cascadia Subduction Zone from Amphibious Seismic Data*. Columbia University.

Jin, G., & Gaherty, J. B. (2015). Surface wave phase-velocity tomography based on multichannel cross-correlation. *Geophysical Journal International*, *201*(3), p. 1383–1398. https://doi.org/10.1093/gji/ggv079

Jin, G., Gaherty, J. B., Abers, G. A., Kim, Y., Eilon, Z., & Buck, R. W. (2015). Geochemistry, Geophysics, Geosystems. *Geochemistry Geophysics Geosystems*, *16*(1–2), p. 3808–3824. https://doi.org/10.1002/2014GC005684.Key

Kasbohm, J., & Schoene, B. (2018). Rapid eruption of the Columbia River flood basalt and correlation with the mid-Miocene climate optimum. *Science advances*, *4*(9), eaat8223.

Kiser, E., Palomeras, I., Levander, A., Zelt, C., Harder, S., Schmandt, B., … Ulberg, C. (2016). Magma reservoirs from the upper crust to the Moho inferred from high-resolution Vp and Vs models beneath Mount St. Helens, Washington State, USA. *Geology*, *44*(6), p. 411–414. https://doi.org/10.1130/G37591.1

Korosec, M.A., 1989, New K-Ar age dates, geochemistry, and stratigraphic data for the Indian Heaven Quaternary volcanic field, south Cascade Range, Washington: Washington Division of Geology and Earth Resources Open-File Report 89-3, p. 42.

Leeman, W. P., Smith, D. R., Hildreth, W., Palacz, Z., & Rogers, N. (1990). Compositional diversity of late Cenozoic basalts in a transect across the southern Washington Cascades: implications for subduction zone magmatism. *Journal of Geophysical Research: Solid Earth*, *95*(B12), p. 19561-19582.

Leeman, W. P., Tonarini, S., Chan, L. H., & Borg, L. E. (2004). Boron and lithium isotopic variations in a hot subduction zone—the southern Washington Cascades. *Chemical Geology*, *212*(1), p. 101-124.

Lees, J. M., & Crosson, R. S. (1989). Tomographic Inversion for Three-Dimensional Velocity Structure at Mount St . Helens Using Earthquake Data. *Journal of Geophysical Research*, *94*, p. 5716–5728. https://doi.org/10.1029/JB094iB05p05716

Lin, F. C., & Ritzwoller, M. H. (2010). Empirically determined finite frequency sensitivity kernels for surface waves. *Geophysical Journal International*, *182*(2), p. 923–932. https://doi.org/10.1111/j.1365-246X.2010.04643.x

Luo, Y., Yang, Y., Xu, Y., Xu, H., Zhao, K., & Wang, K. (2015). On the limitations of interstation distances in ambient noise tomography. *Geophysical Journal International*, *201*(2), p. 652–661. https://doi.org/10.1093/gji/ggv043

Mann, M.E., G.A. Abers, K.J. Crosbie, K.C. Creager, C. Ulberg, S. Moran, and S. Rondenay (2018). “Imaging Subduction beneath Mount St. Helens: Implications for Slab Dehydration and Magma Transport.” *Geophys. Res. Let.*, subm.

McCarthy, C., and Y. Takei (2011), Anelasticity and viscosity ofpartially molten rock analogue: Toward seismic detection ofsmall quantities ofmelt, Geophys. Res. Lett., 38, p. L18306, doi:10.1029/2011GL048776. 1.

McCrory, P. A., Blair, J. L., Waldhauser, F., & Oppenheimer, D. H. (2012). Juan de Fuca slab geometry and its relation to Wadati-Benioff zone seismicity. *Journal of Geophysical Research:*

Solid Earth, *117*(9), p. 1–24. https://doi.org/10.1029/2012JB009407

Menke W. (1989). Geophysical Data Analysis: Discrete Inverse Theory (New York: Acaddemic).

Mitchell, R.J., Jaeger, D.J., Diehl, J.F., and Hammond, P.E., 1989, Paleomagnetic results from the Indian Heaven volca- nic field, south-central Washington: Geophysical Journal, v. 97, p. 381-390.

Mullineaux, D. R. (1996). *Pre-1980 tephra-fall deposits erupted from Mount St. Helens, Washington* (No. 1563).

Obrebski, M., Abers, G. A., & Foster, A. (2015). Magmatic arc structure around Mount Rainier, WA, from the joint inversion of receiver functions and surface wave dispersion. *Geochemistry Geophysics Geosystems*, *16*, p. 178–194. https://doi.org/10.1002/2014GC005581.Received

Pallister, J. S., Thornber, C. R., Cashman, K. V., Clynne, M. A., Lowers, H., Mandeville, C. W., ... & Meeker, G. P. (2008). *Petrology of the 2004-2006 Mount St. Helens lava dome--implications for magmatic plumbing and eruption triggering: Chapter 30 in A volcano rekindled: the renewed eruption of Mount St. Helens, 2004-2006* (No. 1750-30, pp. 647-702). US Geological Survey.

Parsons, T., Wells, R. E., Fisher, M. A., & Flueh, E. (1999). Three-dimensional velocity structure of Siletzia and other accreted terranes in the Cascadia forearc of Washington, *104*, p. 15–18.

Phillips, B. A., Kerr, A. C., Mullen, E. K., & Weis, D. (2017). Lithos Oceanic ma fi c magmatism in the Siletz terrane , NW North America : Fragments of an Eocene oceanic plateau ? *LITHOS*, p. *274–275*, 291–303. https://doi.org/10.1016/j.lithos.2017.01.005

Pollack, H. N., Hurter, S. J., & Johnson, J. R. (1993). Heat flow from the Earth's interior: analysis of the global data set. *Reviews of Geophysics*, *31*(3), p. 267-280.

Porritt, R. W., Allen, R. M., Boyarko, D. C., & Brudzinski, M. R. (2011). Investigation of Cascadia segmentation with ambient noise tomography. *Earth and Planetary Science Letters*, *309*(1-2), p. 67-76.

Reed, J.C, Wheeler, J.O. & Tucholke, B.E., compilers, (2004). Geologic Map of North America:

Decade of North American Geology Continental Scale Map 001, Boulder, Geological Society of America, scale 1:5,000,000.

Schmandt, B., & Humphreys, E. (2011). Seismically imaged relict slab from the 55 Ma Siletzia accretion to the northwest United States, (2), p. 175–178. https://doi.org/10.1130/G31558.1

Schuster, J. Eric. *Geologic map of Washington state*. Washington State Department of Natural Resources, 2005.

Scott, K.M., 1988, Origins, behavior, and sedimentology of lahars and lahar-runout flows in the Toutle-Cowlitz River system: U.S. Geological Survey Professional Paper 1447-A, p. 76.

Scott, K.M., 1989, Magnitude and frequency of lahars and lahar-runout flows in the Toutle-Cowlitz River system: U.S. Geological Survey Professional Paper 1447-B, p. 33.

Shapiro, N. M., & Campillo, M. (2004). Emergence of broadband Rayleigh waves from correlations of the ambient seismic noise. *Geophysical Research Letters*, *31*(7), p. 8–11. https://doi.org/10.1029/2004GL019491

Shen, W., Ritzwoller, M. H. & Schulte-Pelkum, V. A 3-D model of the crust and uppermost mantle beneath the Central and Western US by joint inversion of receiver functions and surface wave dispersion. J. Geophys. Res.-Sol. Earth 118, 262–276 (2013). p. 17.

Shen, W., & Ritzwoller, M. H. (2016). Journal of Geophysical Research : Solid Earth, p. 1–37. https://doi.org/10.1002/2016JB012887.Received

Sisson, T. W., Salters, V. J. M., & Larson, P. B. (2014). Petrogenesis of Mount Rainier andesite: Magma flux and geologic controls on the contrasting differentiation styles at stratovolcanoes of the southern Washington Cascades. *Bulletin of the Geological Society of America*, *126*(1–2), p. 122–144. https://doi.org/10.1130/B30852.1

Smith, D.R., and Leeman, W.P., 1993, The origin of Mount St. Helens andesites: Journal of Volcanology and Geothermal Research, v. 55, p. 271-303.

Stanley, W. D., Finn, C., & Plesha, J. L. (1987). Tectonics and conductivity structures in the Southern Washington Cascades. *Journal of Geophysical Research: Solid Earth*, *92*(B10), p. 10179–10193. https://doi.org/10.1029/JB092iB10p10179

Stanley, W. D., Johnson, S. Y., Qamar, A. I., Weaver, C. S., & Williams, J. M. (1996). Tectonics and seismicity of the southern Washington Cascade range. *Bulletin of the Seismological Society of America*, *86*(1 SUPPL. A), p. 1–18.

Swanson, D.A., 1989, Geologic maps of the French Butte and Greenhorn Buttes quadrangles, Washington: U.S. Geologi- cal Survey Open-File Report p. 89-309, 25, scale 1:24,000.

Swanson, D.A., 1994, Geologic map of the East Canyon Ridge quadrangle, southern Cascade Range, Washington: U.S. Geological Survey Open-File Report p. 94-591, 31.

Syracuse, E. M., & Abers, G. A. (2006). Global compilation of variations in slab depth beneath arc volcanoes and implications. *Geochemistry, Geophysics, Geosystems*, *7*(5). https://doi.org/10.1029/2005GC001045

Syracuse, E. M., van Keken, P. E., Abers, G. A., Suetsugu, D., Bina, C., Inoue, T., … Jellinek, M. (2010). The global range of subduction zone thermal models. *Physics of the Earth and Planetary Interiors*, *183*(1–2), p. 73–90. https://doi.org/10.1016/j.pepi.2010.02.004

Tatsumi, Y., Shukuno, H., Tani, K., Takahashi, N., Kodaira, S., & Kogiso, T. (2008). Structure and growth of the Izu-Bonin-Mariana arc crust: 2. Role of crust-mantle transformation and the transparent Moho in arc crust evolution. *Journal of Geophysical Research: Solid Earth*, *113*(2). https://doi.org/10.1029/2007JB005121

Till, C.B., Kent, A.J.R., Abers, G.A., Janiszewski, H.A., Gaherty, J.B., Pitcher, B.W. (2018). Towards Assessing the Causes of Volcanic Diversity at the Arc Scale. *Nature Communications,* in review.

Ulberg, C.W., Creager, K.C., Moran, S.C., Abers, G.A., Levander, A., Schmandt, B., Hansen, S., Crosson, R. (2018). Local earthquake *Vp* and *Vs* tomography in the Mount St Helens region with the iMUSH broadband array. *Journal of Geophysical Research,* in prep.

Valley, P. M., Whitney, D. L., Paterson, S. R., Miller, R. B., & Alsleben, H. (2003). Metamorphism of the deepest exposed arc rocks in the Cretaceous to Paleogene Cascades belt, Washington: evidence for large-scale vertical motion in a continental arc. *Journal of Metamorphic Geology*, *21*(2), p. 203-220.

van Keken, P. E., Wada, I., Abers, G. A., Hacker, B. R., & Wang, K. (2018). Mafic High-Pressure Rocks Are Preferentially Exhumed From Warm Subduction Settings. *Geochemistry, Geophysics, Geosystems*, *19*(9), p. 2934-2961.

Wada, I., & Wang, K. (2009). Common depth of slab-mantle decoupling: Reconciling diversity and uniformity of subduction zones. *Geochemistry, Geophysics, Geosystems*, *10*(10).

Wagner, L., Forsyth, D. W., Fouch, M. J., & James, D. E. (2010). Detailed three-dimensional shear wave velocity structure of the northwestern United States from Rayleigh wave tomography. *Earth and Planetary Science Letters*, *299*(3–4), p. 273–284. https://doi.org/10.1016/j.epsl.2010.09.005

Waite, G. P., & Moran, S. C. (2009). VP Structure of Mount St. Helens, Washington, USA, imaged with local earthquake tomography. *Journal of Volcanology and Geothermal Research*, *182*(1–2), p. 113–122. https://doi.org/10.1016/j.jvolgeores.2009.02.009

Walowski, K. J., Wallace, P. J., Hauri, E. H., Wada, I., & Clynne, M. A. (2015). Slab melting beneath the Cascade Arc driven by dehydration of altered oceanic peridotite. *Nature Geoscience*, *8*(5), p. 404.

Wang, Y., Lin, F. C., Schmandt, B., & Farrell, J. (2017). Ambient noise tomography across Mount St. Helens using a dense seismic array. *Journal of Geophysical Research: Solid Earth*, *122*(6), p. 4492-4508.

Ward, K. M., Zandt, G., Beck, S. L., Christensen, D. H., & McFarlin, H. (2014). Seismic imaging of the magmatic underpinnings beneath the Altiplano-Puna volcanic complex from the joint inversion of surface wave dispersion and receiver functions. *Earth and Planetary Science Letters*, *404*, p. 43–53. https://doi.org/10.1016/j.epsl.2014.07.022

Weaver, B. L., Wood, D. A., Tarney, J., & Joron, J. L. (1987). Geochemistry of ocean island basalts from the south Atlantic: Ascension, Bouvet, St. Helena, Gough and Tristan da Cunha. *Geological Society, London, Special Publications*, *30*(1), p. 253-267.

Wells, R., Bukry, D., Friedman, R., Pyle, D., Duncan, R., Haeussler, P., & Wooden, J. (2014). Geologic history of Siletzia, a large igneous province in the Oregon and Washington Coast

Range: Correlation to the geomagnetic polarity time scale and implications for a long-lived Yellowstone hotspot. *Geosphere*, *10*(4), p. 692–719. https://doi.org/10.1130/GES01018.1

Wheeler, J.O. (2004). Geology of Canda, Greenland, Iceland, and parts of Ireland for the Geologic Map of North Aerica, in Reed, John C. Jr., Wheeler, John. O., and Tucholke, Brian E., compilers, 2004. Geologic Map of North America: Decade of North American Geology Continental Scale Map 001, Boulder, Geological Society of America, scale 1:5,000,000.

Yao, Z. S., Roberts, R. G., & Tryggvason, A. (1999). Calculating resolution and covariance matrices for seismic tomography with the LSQR method. *Geophysical Journal International*, *138*(3), p 886–894. https://doi.org/10.1046/j.1365-246X.1999.00925.x

Zhou, Y., Dahlen, F. A., Nolet, G., & Laske, G. (2005). Finite-frequency effects in global surface-wave tomography, p. 1087–1111. https://doi.org/10.1111/j.1365-246X.2005.02780.x

APPENDIX A

DATA QUALITY CONTROL, DATA COMBINATION, AND RESOLUTION TESTS

A.1 Feature Recovery Resolution Tests

Feature recovery tests in addition to the checkerboard tests and E-W boundary in the main text (Figures 2.4-2.5) were done to test recovery of small squares of low velocity at 0.18 Hz. This geometry approximates the previously observed upper-crustal magma chamber at about 8-10 km depth (Waite and Moran, 2009). The square anomaly is input, and synthetic data is solved for using the finite-frequency kernels, which is then input into the inversion with the same damping parameters as the real inversion process. If the block is 5 km x 5 km, the peak amplitude is 19% recovered, and a 10 km x 10 km chamber is 47 % recovered, comparing the peak of the model to the maximum synthetic model perturbation.

A square -10% phase velocity block, 30 km wide at frequencies 0.05-0.1 Hz, is input into the inversion. This is meant to imitate a lower crustal partial melt zone. The feature has a peak recovery of 40% of the maximum perturbation at 0.06 Hz. It is very difficult to detect at 0.05 Hz.

A.2 Phase Velocity Data Combination of Surface Wave Earthquake Tomography and Ambient Noise Tomography at 0.05 Hz

Individual phase velocity datasets at 0.05 Hz from ambient noise and regional surface wave earthquake tomography from Janiszewski et al. (2018) are combined for the final phase velocity map. It was thought that the iMUSH dataset was well resolved inside the array and so the iMUSH data should be used there and outside the array the regional data would be used. A 2D cosine window, *W,* (Figure A.4a), which tapers from the origin, and a constant s=0.2 are used to weight the combination of the phase velocities from ambient noise (V_{ANT}) and the regional EQ surface wave data (V_R) as follows:

$$V_{tot} = (W * V_{ANT} + s * V_R)/(s + W) \quad \text{(eq. A.1)}$$

The earthquake datasets have significantly lower uncertainties than the ambient noise, although the resolution of the ambient noise is much better. The uncertainties of the earthquake datasets are

scaled up by $1/s = 5$ in the *Vs* inversion to stabilize the mismatch in resolution and the concern that the uncertainties are calculated in different ways. The uncertainties of the phase velocity combination are propagated (after scaling the regional earthquake uncertainties up by s) as follows:

$$\sigma_{tot} = \sqrt{(W/(s+W))^2 * \sigma_{ANT}^2 + (s/(s+W))^2(5\sigma_R)^2)} \qquad \text{(eq. A.2)}$$

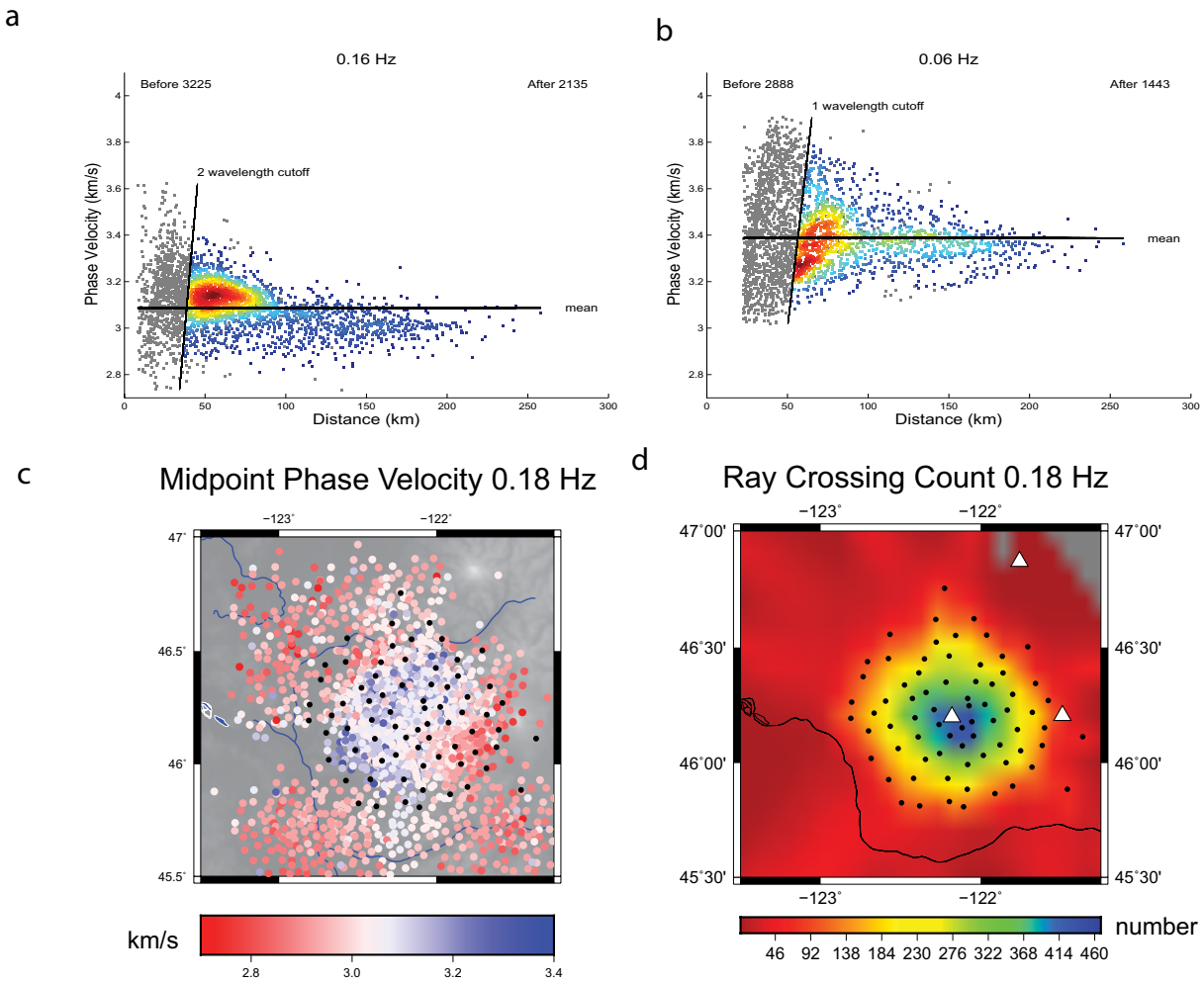

Figure A.1: Phase velocities at all station pairs, plotted with interstation distance for two frequencies, 0.16 Hz (**a**) and 0.06 Hz (**b**). Color shows density of points. Grey points are data that are not used due short distance or phase velocities being 3 median absolute deviations above the median, where the median absolute deviation is calculated for 1-2 cycles, 2-3 cycles, and above 3 cycles. Black like shows distance cutoff as a minimum number of cycles. **c:** Phase velocities for 0.18 Hz plotted at the midpoint of station pairs. **d:** Ray density per 5 km x 5 km pixel.

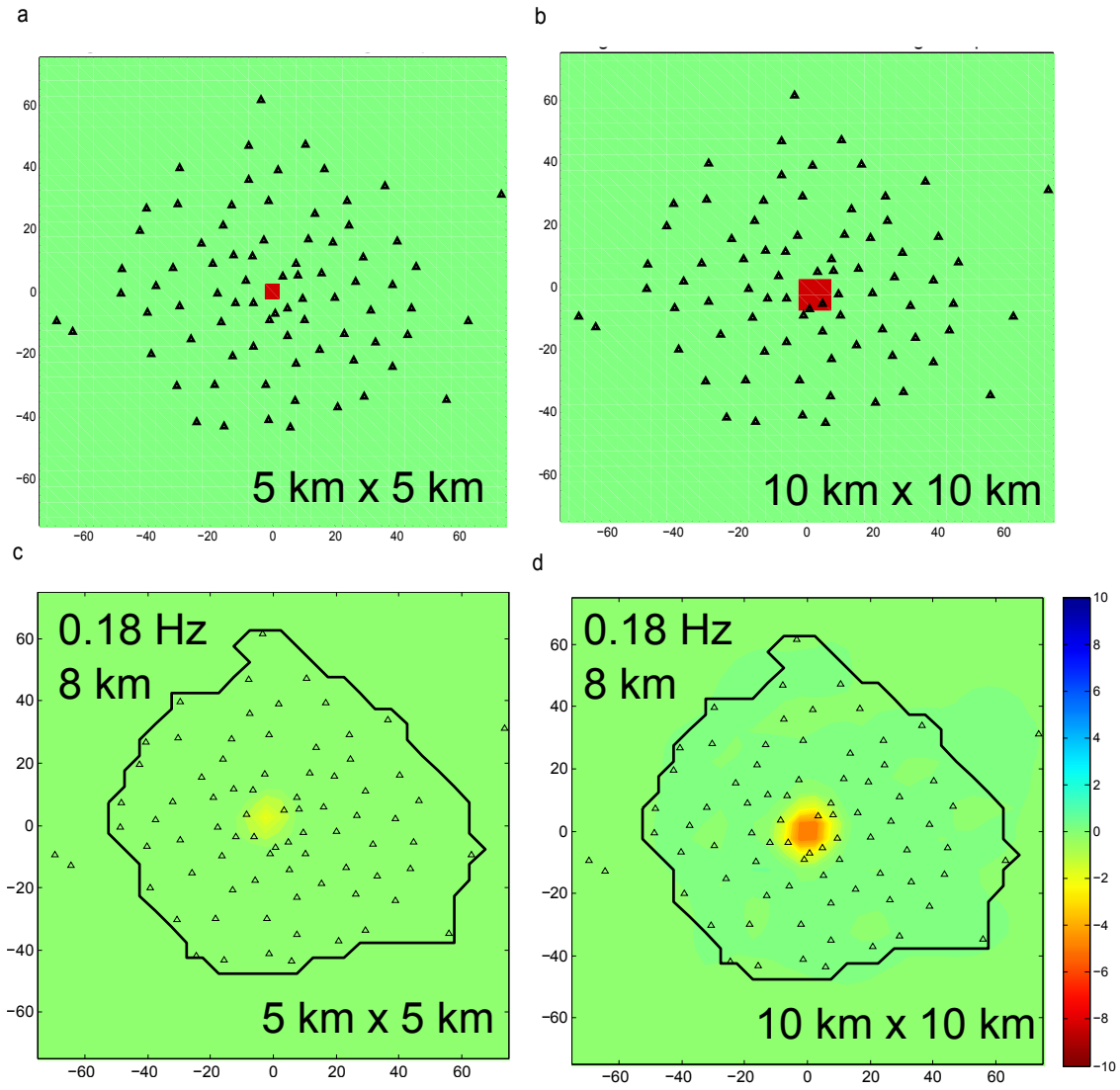

Figure A.2: A recovery test for a small square low-velocity anomaly at 0.18 Hz. **a:** The input -10% velocity block, 5x5 km in dimension. **b:** input feature for 10x10 km block. **c:** inversion result for the 5x5 km block. **d:** inversion result for 10x10 km block. In each panel, the black triangles are stations and the thick lack line is the resolution contour from 0.1 Hz.

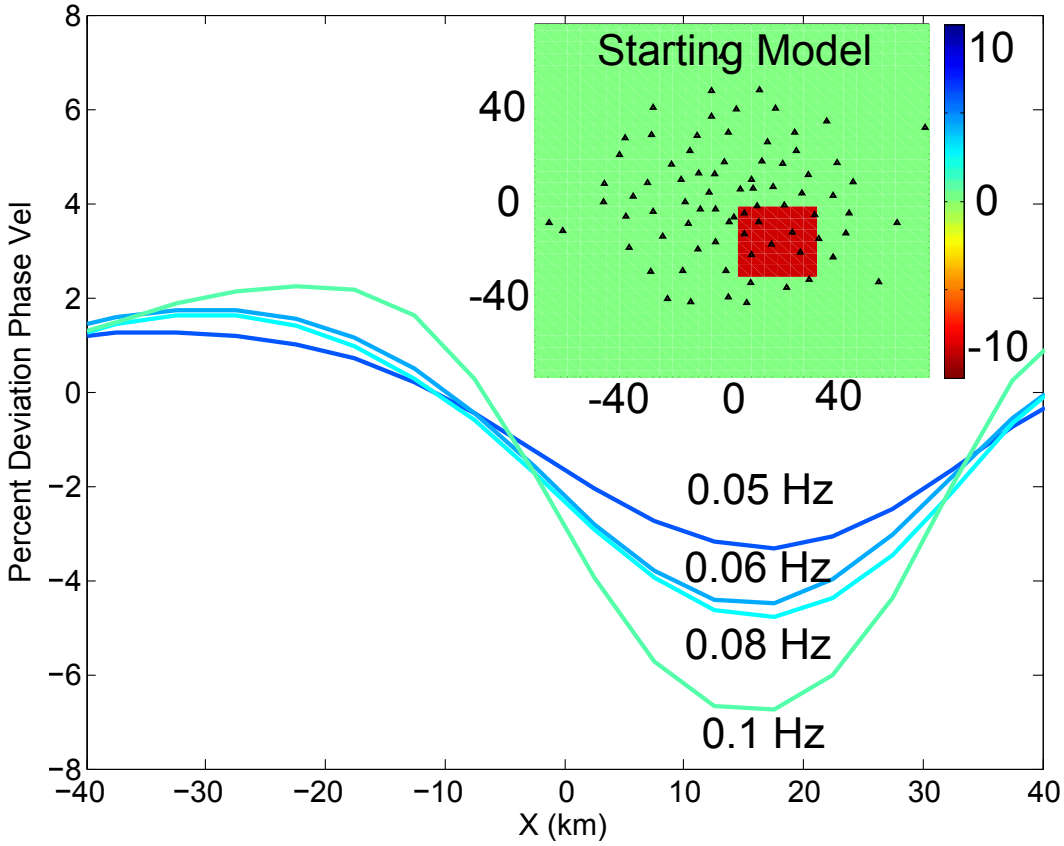

Figure A.3: The recovery of a 30 km x 30 km low-velocity square phase-velocity anomaly depicted in **inset**, with a -10% phase velocity perturbation, for frequencies 0.05-0.1 Hz. The recovered anomaly is plotted on an E-W transect through the center of the low velocity zone showing percent deviation in phase velocity output. X=0 is the longitude of Mount St. Helens and the triangles are the stations. Anomaly geometry approximates a lower crustal partial melt zone as in Kiser et al., (2016)

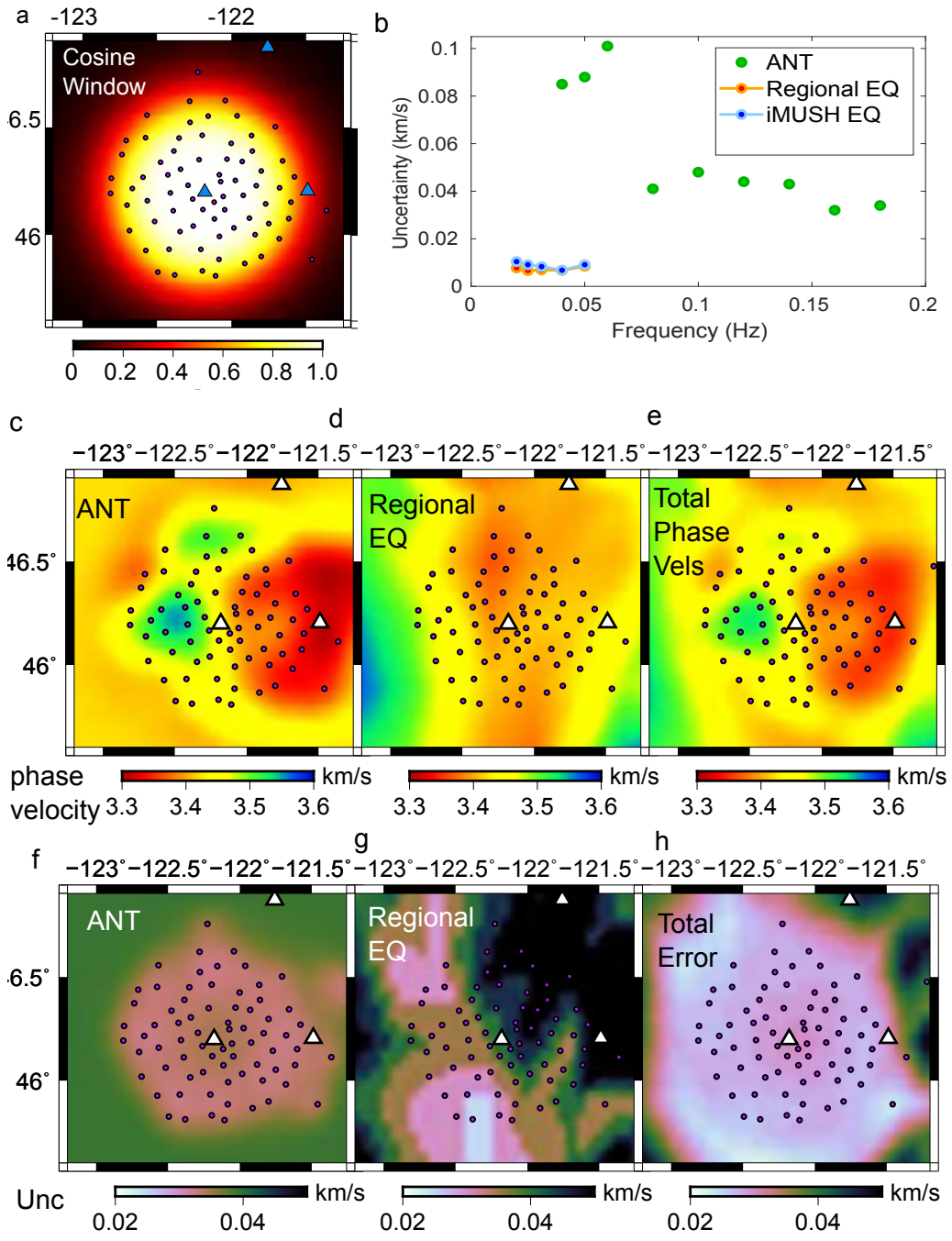

Figure A.4: a: The cosine window used to combine the data. **b:** The average uncertainties for the ambient noise, iMUSH, and regional earthquake data. It is clear that the uncertainties are very different between ambient noise and earthquake methods. **c:** The ambient noise phase velocity map for 0.05Hz. **d:** The regional earthquake phase velocity map for 0.05 Hz. e: The combination of those two datasets using the method described in the appendix. **f-h:** The uncertainties for the same datasets as **c-e** respectively, where the regional earthquake uncertainties have been scaled up by 5.

APPENDIX B: BEAMFORMING FOR DIRECTIONALITY AND AVERAGE PHASE VELOCITY

We use beamforming to independently constrain the sources of coherent ambient noise and the stability of phase velocities measured from it (e.g., Gertsoft et al., 2006; Harmon et al., 2008). Beamforming gives an average phase velocity and directionality from the coherence of plane wave signals across the array. These estimates are based on background noise in 512 s time windows, formed into beams over a grid of trial slowness vectors and then stacked monthly, subsequently stacked over a full year to sample annually-averaged noise. Beams are formed in a manner similar to Harmon et al. (2008); preprocessing includes narrow-band filtering of continuous time series at multiple frequencies between 0.05 and 0.18 Hz, detrending and windowing each 512 s segment. To remove earthquakes, the signals are clipped above four times the median standard deviations of all segments in the same time window, and then gain is normalized by this same factor. Phase delays are calculated from the cross-spectral density matrix across the array, giving a beam power at each slowness and azimuth (Harmon et al., 2008). Phase velocity and uncertainty, shown on Figure 2.2d, is estimated from the beamformer output by fitting a Gaussian model of noise coherence that varies only with slowness.

Overall the beams (Figure B.1) show close agreement with array-averaged $c(\omega)$ estimated from ambient noise, to within 0.01 km/s at 0.05-0.18 Hz (Figure 1.4; section 2.2.3). Lower frequencies naturally show broader peaks. At most frequencies the noise from west to northwestern back-azimuths dominates, probably reflecting the high energy in high-latitude microseismic noise sources (Ardhuin et al., 2011). A secondary southeastern back azimuth is persistent at many frequencies. Overall the noise wavefield is not strongly directional, so the fundamental assumptions in ANT seem valid here.

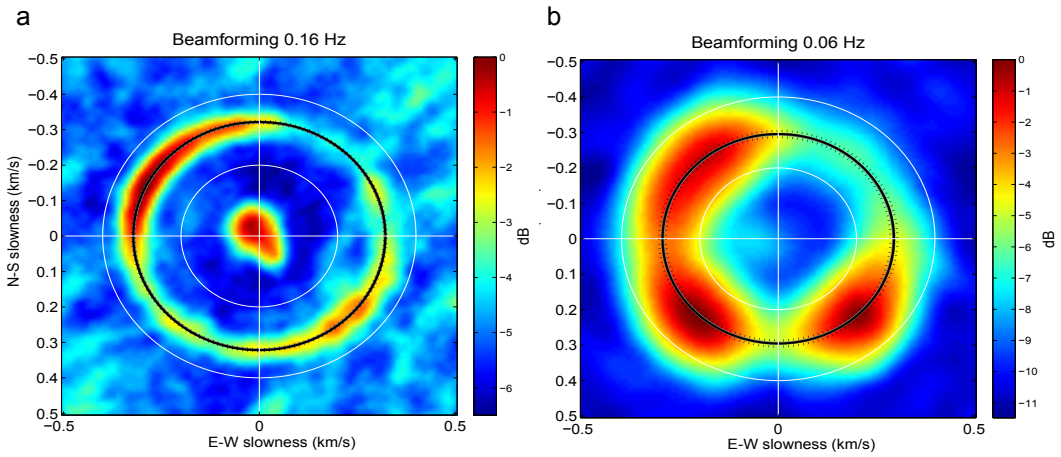

Figure B.1: Beam power at each vector slowness for 10 months of data at two example frequencies, 0.16 Hz (**a**) and 0.06 Hz (**b**). Black circle shows best-fit to peak from fitting a Gaussian model to power distribution, and is used to estimate phase velocities on **Figure 2.4b**.

APPENDIX C: GENERALIZED CROSS VALIDATION TEST FOR SMOOTHING PARAMETER IN 2D AMBIENT NOISE PHASE VELOCITY TOMOGRAPHY AND INVERSION STATISTICS AND THEORY

Appendix C.1 Inversion Theory

Theory for the ambient noise finite frequency inversion is clearly outlined in the TOMO2D/ rayinvert2d manual (G. Abers, unpub. Software manual, 2018). Here we briefly cover the theory of the inversion. The inversion is a single-step, linear inversion of station pair-wise travel time data, which solves for a model of perturbations to slowness at nodes on a grid. The travel time data is station pair-wise travel time delays from ambient noise. The model, *m,* is solved as follows:

$$m = [G^T G + p^{-2}(M_m + fI)]^{-1} G^T d \qquad \text{(eq. C.1)}$$

where G is the kernel, p is the smoothing parameter, M_m is the unscaled first-derivative smoothing matrix, f is the rescaling factor for model norm damping, and d is the uncertainty-weighted travel

time residual. The kernel G is defined as follows:

$$G_{ij} = (dt_i/dm_j)/\sigma_i \quad \text{(eq. C.2)}$$

a derivative matrix scaled by data uncertainties. Data is scaled by uncertainties like this:

$$d_i = (t_i - t_i^p)/\sigma_i \quad \text{(eq. C.3)}$$

where t_i is travel time for the i^{th} station pair, s_i is the data uncertainty, and t^{pred} is the predicted travel time for the starting model:

$$t_i^p = \Delta_i/v_{ref} \quad \text{(eq. C.4)}$$

where D_i is the distance between the i^{th} pair of stations and v_{ref} is the reference velocity, an average of the network. The reference velocity is calculated as follows:

$$v_{ref} = \frac{\sum \Delta_i/\sigma_i}{\sum t_i/\sigma_i} \quad \text{(eq. C.5)}$$

The kernel, G, is scaled by the covariance matrix:

$$G^T G = A^T C_d^{-1} A \quad \text{(eq. C.6)}$$

where A is the same as G without the uncertainty weighting.

Appendix C.2 GCV Test

The standard L-curve analysis (Menke, 1989) was inconclusive in determining a smoothing parameter for the 2D inversion for phase velocities. Instead the generalized cross validation (GCV) function method was used to determine smoothing parameters (Inoue et al., 1990; Yao & Robert, 1999). Specifically, the damping value, *p,* was determined by this method at two end member frequencies and is the red point in Figure C.1. The inversion is repeated after omitting 100 different subsets, that add up to the full dataset, of the data for each smoothing parameter. The misfit is calculated between the omitted data and the predicted data based on the model without the data. This misfit is normalized and summed for all iterations, and the minimum with respect to smoothing parameter, *p*, of this misfit is the point of optimal smoothing. Smoothing parameters are linearly interpolated between the two end-member smoothing parameters determined for 0.06 Hz and 0.18 Hz in this manner, and linearly extrapolated to 0.05 Hz (Table C.1).

As described in C.1 the data used in the inversion are two-station travel-times (*t*), derived

from phase velocity measurements at a given frequency. The data that is omitted is travel time data *t* and is normalized by the travel time error as in equation C.3, where t^{pred} is calculated as in equation C.4.

Then the predicted data from the solution *m* (which is the model of slownesses) calculated without the omitted data *d* and the *G* matrix with spatial information based on the omitted data is calculated:

$$d^p = Gm \qquad \text{(eq. C.7)}$$

The G matrix is calculated in equation C.2. Then the misfit between this predicted data and the omitted data is calculated as follows:

$$\sigma = \frac{\sqrt{\sum (d - d^p)^2}}{\sum (t/t^{error})^2} \qquad \text{(eq. C.8)}$$

This misfit is calculated for 100 subsets and then summed

$$\sigma_{tot} = \sum \sigma \qquad \text{(eq. C.9)}$$

Finally, this is normalized by the trace of the identity minus the data importance matrix GG^{-g}

$$GCV(p) = \frac{\sigma_{tot}}{trace(I - GG^{-g})} \qquad \text{(eq. C.10)}$$

where the data importance matrix is calculated as follows:

$$GG^{-g} = G(G^T G + \frac{1}{p^2} H^T H + \frac{f}{p^2} I)^{-1} G^T \qquad \text{(eq. C.11)}$$

where p is the smoothing parameter, *f* is the multiplicative factor to the smoothing parameter to get the model norm damping, and $H^T H$ is the first derivative smoothing matrix. The GCV is calculated for each smoothing parameter and the minimum of the GCV gives the optimal smoothing parameter.

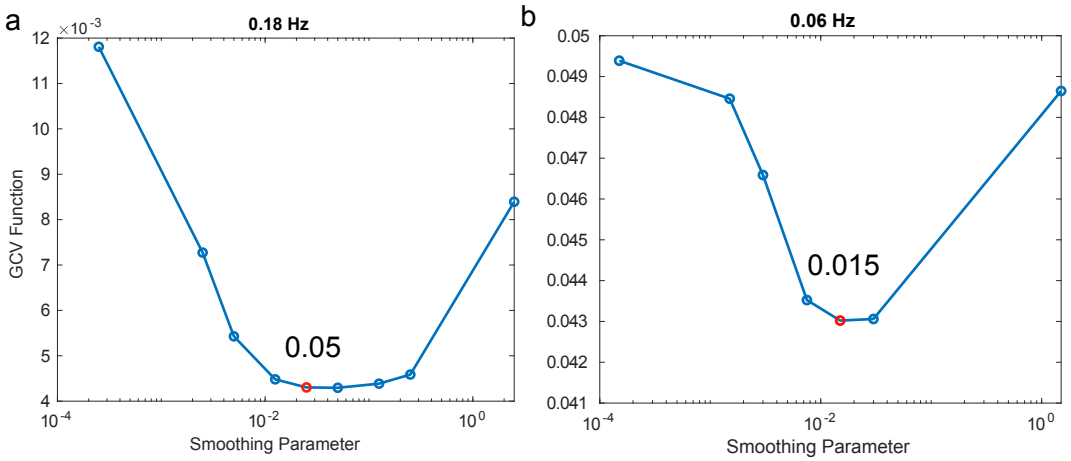

Figure C.1: The GCV function used to determine optimal damping parameter, p, for the 2D phase velocity inversions, at two end member frequencies of 0.18 Hz (**a**) and 0.06 Hz (**b**). The minimum of the GCV function determines the optimal damping values (red point). The GCV function and method is described in the text for Appendix C.

Table C.1: Ambient Noise 2D Inversion Statistics and Parameters[1]
[2]

Frequency (Hz)	Model Norm Damping (s/km)	Smoothing (s/km)	Prior Error Scaling Factor	Variance (s^2)	Variance reduction	Model Size $(s/km)^2$	Max Kernel Diagonal $(s/km)^2$	Chi-Squared Factor
0.05	1.21E-04	0.0121	4.32E-02	0.479	26.0%	3.63E-05	6.2E+05	1.11
0.06	1.50E-04	0.015	7.68E-02	0.497	24.4%	8.13E-05	3.98E+05	1.09
0.08	2.08E-04	0.0208	3.50E-02	0.165	64.4%	8.66E-04	3.98E+05	1.15
0.1	2.67E-04	0.0267	6.44E-02	0.17	57.1%	1.21E-03	1.31E+05	1.15
0.12	3.25E-04	0.0325	6.44E-02	0.115	59.9%	1.99E-03	1.01E+05	1.15
0.14	3.83E-04	0.0383	6.44E-02	0.07	68.4%	2.66E-03	9.09+04	0.96
0.16	4.42E-04	0.0442	5.03E-02	0.048	78.9%	7.02E-03	1.22E+05	1.13
0.18	5.00E-04	0.05	5.00E-02	0.049	81.5%	9.38E-03	1.27E+05	1.11

[1] Table C.1: Model norm damping limits the extrapolation of the model outside the area of resolution and keeps it close to the array average slowness. Smoothing parameter gives the amount of first derivative smoothing. Prior error scaling scales the travel time errors to a value that gives correct uncertainties out and so that the variances follow a chi-squared distribution. This should make the chi-squared factor as close to 1 as possible. Variance is the variance of the residuals and the variance reduction is the reduction from the data variance to the residual variance. Model size is the size of the model of slownesses. The max kernel diagonal is the largest diagonal on the G matrix, which tells us if a large or small number is added to it with the model norm damping.

APPENDIX D: COMPLETE VS MODEL AND VS MODEL WITH MOHO MODEL

The *Vs* model was calculated for a model with a Moho (the "Moho" model) and without a Moho (the "gradient" model) to see the sensitivity of *Vs* structure to starting model. Table D.1 has these two models from the network-averaged phase velocity fits and their uncertainties (Figure 2.2).

The transects in Figure 1.13 are calculated with a gradient model and these same transects are shown in Figure D.1 but with a Moho model. The Moho is much stronger in these figures.

In Figure 2.8 only 6 *Vs* depth slices are shown. In Figure D.2 we show all calculated *Vs* slices. There are maps every 2.5 km down to 20 km, and every 5 km down to 110 km. The middle of the depth slice is labeled in the figure.

Table D.1: 1D *Vs* Starting Models

	Gradient model		Moho model	
Depth (km)	Vs (km/s)	Uncertainty (km/s)	Vs (km/s)	Uncertainty (km/s)
0	3.21	0.14	3.21	0.13
2.5	3.35	0.12	3.36	0.10
5	3.36	0.08	3.37	0.07
7.5	3.39	0.12	3.39	0.11
10	3.52	0.07	3.52	0.10
12.5	3.64	0.11	3.64	0.07
15	3.64	0.07	3.65	0.06
17.5	3.62	0.11	3.63	0.08
22.5	3.67	0.11	3.67	0.08
27.5	3.751	0.07	3.71	0.09
32.5	3.81	0.07	2.71	0.09
37.5	4.15	0.11	4.33	0.09
42.5	4.35	0.12	4.0	0.10
47.5	4.39	0.10	4.14	0.10
52.5	4.42	0.13	4.27	10.10
57.5	4.43	0.10	4.41	0.08
62.5	4.44	0.11	4.45	0.08
67.5	4.45	0.11	4.45	0.11
72.5	4.45	0.11	4.45	0.13
77.5	4.45	0.11	4.45	0.13
82.5	4.45	0.11	4.44	0.10

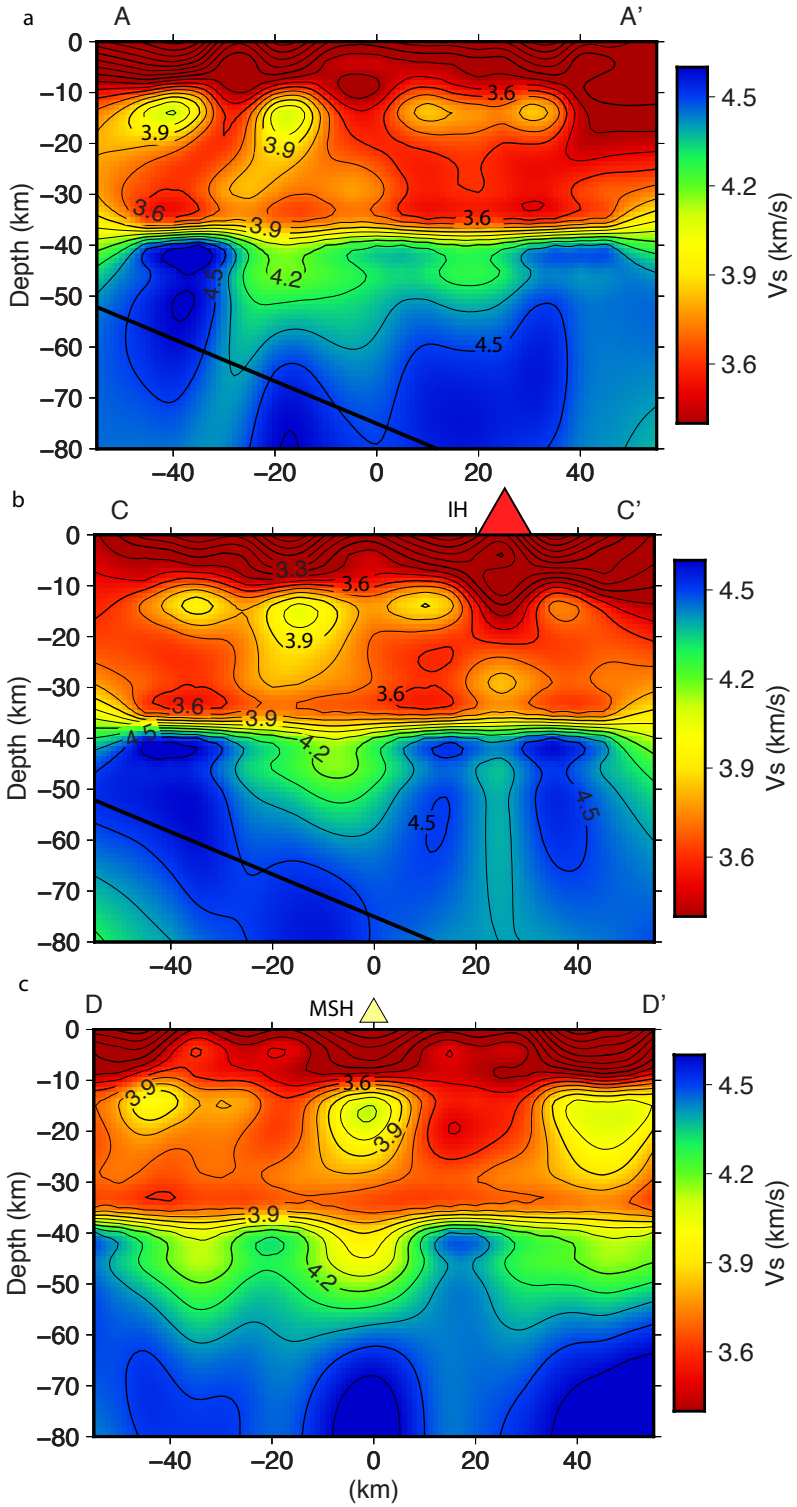

Figure D.1: Cross sections through the *Vs* model for the Moho discontinuity inversions, as **Figure 1.13** with locations of cross sections in **Figure 1.13b**. **a**: cross-section A-A'. **b**: cross-section C-C'. **c**: north-south cross-section D-D'.

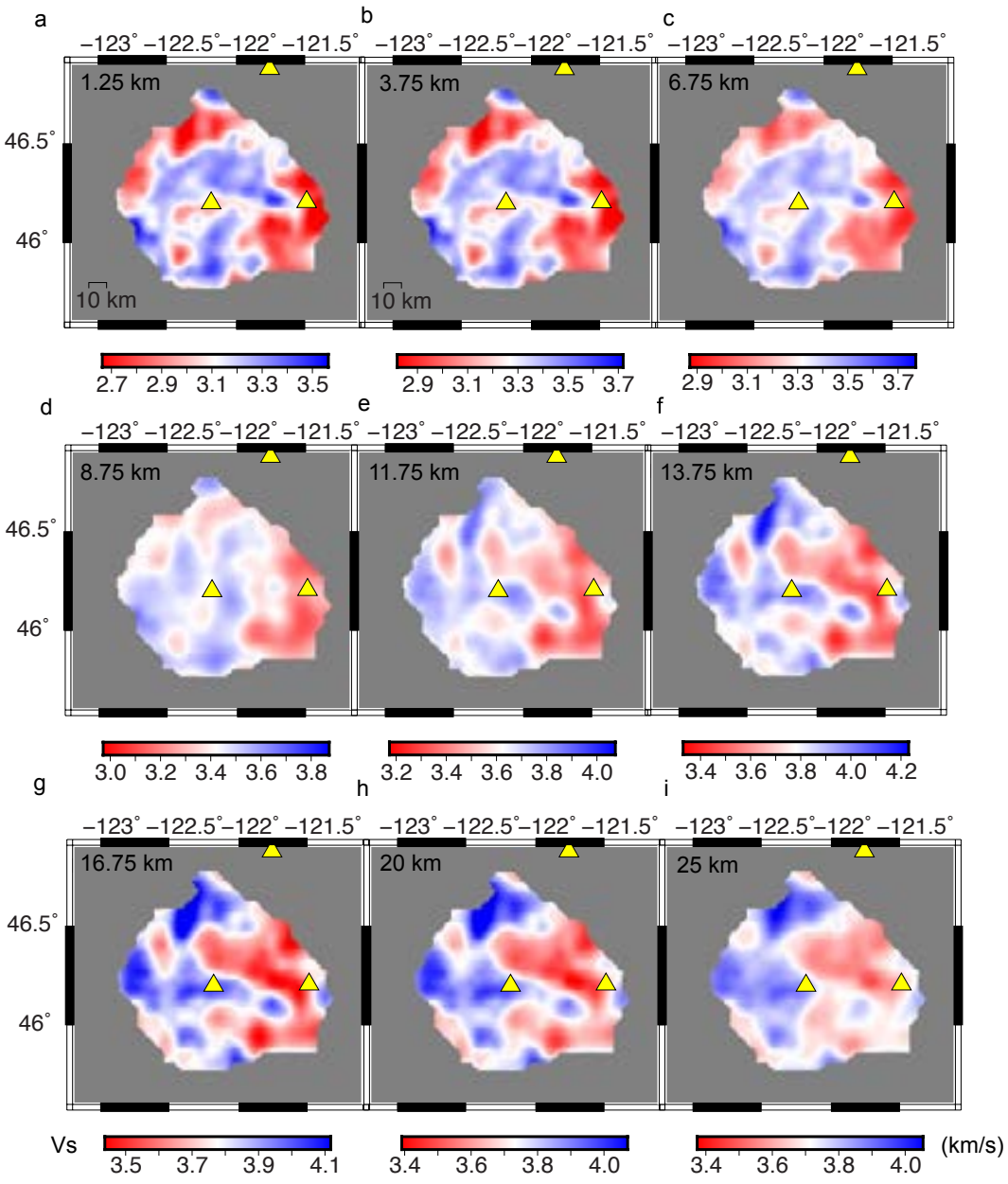
a
b
c
−123˚ −122.5˚−122˚ −121.5˚
1.25 km
3.75 km
6.75 km
46.5˚
46˚
10 km
2.7 2.9 3.1 3.3 3.5
2.9 3.1 3.3 3.5 3.7
2.9 3.1 3.3 3.5 3.7
d
e
f
8.75 km
11.75 km
13.75 km
3.0 3.2 3.4 3.6 3.8
3.2 3.4 3.6 3.8 4.0
3.4 3.6 3.8 4.0 4.2
g
h
i
16.75 km
20 km
25 km
Vs
3.5 3.7 3.9 4.1
3.4 3.6 3.8 4.0
3.4 3.6 3.8 4.0
(km/s)

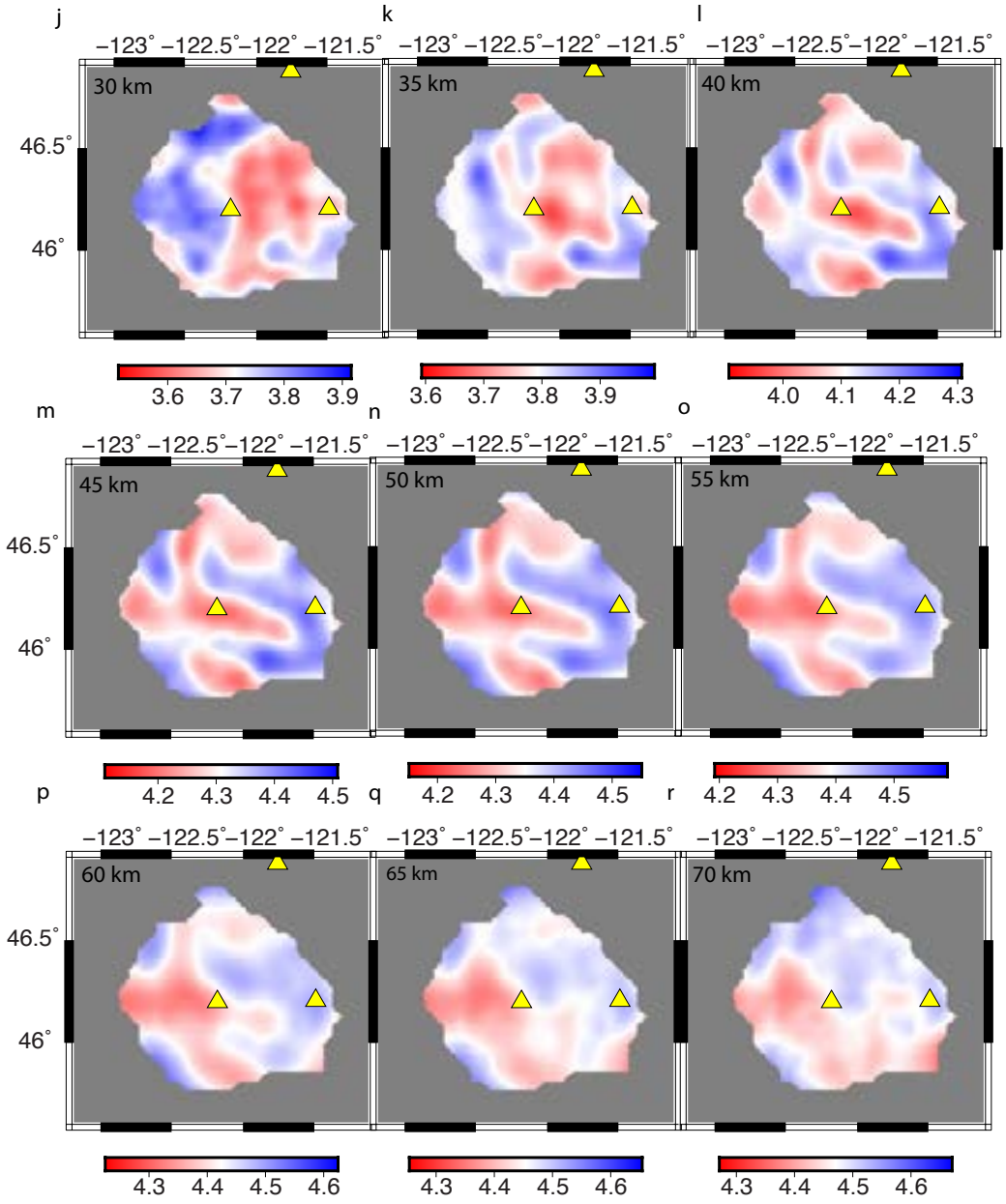

Figure D.2: The complete *Vs* 3D model with a gradient model. Each depth slice center is labeled in the top left corner.

APPENDIX E

LOCATION OF CODES AND DATA ON KONE

Appendix E.1: Location of Matlab Codes

All matlab scripts are located in /home/kjc233/Documents/matlab/

The main directories with scripts are

TOMO2D_v3/	Ambient noise finite frequency tomography scripts
MATNOISE_v3/	Cross correlation codes for ambient noise
MATNOISE_V16/	Spectrum fitting for phase velocities from noise
invertMC/	Monte Carlo codes for Vs uncertainties and Vs inversion
ANT_plotting	Miscellaneous plotting codes after doing ANT
Heatflow_Perplex/	Heatflow and Perplex outputs for Vs of Siletz
Phasevel_combine/	Combines regional EQ surface wave phase velocity with ANT
SWpackage/	Script from Helen Janiszewski for surface wave EQ tomo
Beamforming/	Beamforming scripts and plotting

TOMO2D_v3

Manual written by G Abers on TOMO2D/rayinvert. Extra scripts are loop_iMUSH_rayinvert.m which loops through all frequencies, sets parameters and runs the inversions. Other directories are

GCV_v2/

bootstrapping/

resolution_tests/

test_data_params/

GCV_v2

has scripts from TOMO2D but changed to do GCV analysis, run with **rayinvert_crossval_180m-hz.m** on 180 mhz data, change frequency to do other datasets. Run **calc_GCV.m** on the output mat file to calculate the GCV function.

bootstrapping

Does bootstrapping to calculate error from the ANT tomography to compare with formal uncertainties. Run with **loop_iMUSH_boot.m**

resolution_tests

Does checkerboard test or tests a single block by setting iblob to 0 or 1 respectively in **fwdmod_synth.m** Can set the following parameters for the tests

grd	checkerboard block size in pixels
per	percent deviation in velocity of blocks
width	width of block
height	height of block
xcen	center of block (x) in km
ycen	center of block (y) in km
isneg	block is negative anomaly if 0 and positive if 1

test_data_params

has some test data files and parameterfiles

mn_phvel_jindd2_0.180.data	station-pair wise phase velocities for 0.18 Hz
par_imush	TOMO2D parameters for iMUSH array
stalist_mshall.txt	station list for iMUSH array

MATNOISE_v3

Cross correlation scripts to do ambient noise

includes the directory **MAT_NOISE/** which has important subroutines

important scripts are

matnoise_v33.m	Does the cross correlations
mn_add_ncf_stacks2.m	Takes multiple batches of cross correlations and combines them
mn_dataselect4.m	Does data quality control

Example of how to write scripts and run them in batch mode is all of the scripts in

/ld3/iMUSH/kjc233/xc_UW3/

matnoise_v33_#.m numbered 1-35

And then these are run 4 at a time using **MatnoiseLoop.bash** in /home/kjc233/Documents/data/MSHXCresults/

MATNOISE_V16

This has the scripts to the spectrum fitting of the correlograms to get station pair-wise phase velocities. The important main script is

mn_fitxcspec16.m

And other important subroutines are

j0zeroseries.m	Calculates the j0 Bessel function as a series
j1zeroseries.m	Calculates the j1 Bessel function as a series
mn_bess2phvel.m	gets phase velocities from the Bessel function
mn_zctophvel.m	gets phase velocities from the zero crossings of the Bessel function (old method)
mn_zc2predcurv.m	Gets the dispersion curve prediction from zero

crossings of the Bessel function (old method)

invertMC

Does the Monte Carlo inversions for Vs uncertainty, also drives the 1D single iteration Vs inversions. Reguires a premade directory with the starting model and a subdirectory for each pixel labeled y_x, inside of each is the phase velocity file.

Important driving script is

invert1d_montecar_msh_1D_grad.m for a gradient model

and

invert1d_montecar_msh_1D_moho.m for a Moho model

and other subroutines are:

invdispR_msh.m executes the runfile and does 1D inversion

invdispR_prep_msh_grad.m writes the runfile, does once for all iterations

invdispR_synth.m calculates the synthetic fits for the start model

montecarl_msh1.m perturbs the starting model and runs inversion

plot_monte.m makes a fancy plot of Vs inversion and 1 and 2 sigma uncertainty, phase velocity and 1 std of fits, and histogram of misfits

readdisp_surf96.m reads surf96 phase velocity file

readmod_surf96.m reads surf96 Vs model file

writedisp_surf96.m writes surf96 phase velocity file

writemod_surf96.m write surf96 Vs model file

setup_parameters_msh.m sets up parameters for MC inversion, parameters include:

testN number of MC iterations

velocity_var variance of velocity perturbations

r allowed std of output

ANT_plotting

Some miscellaneous plotting scripts for various ANT outputs, useful ones are

plot_surf96_disp_model_output4.m	plots dispersion curves and 1D Vs output for a 1D inversion
EW_compare_Vs.m	Compares avg Vs as 1D Vs in the east and west of MSH
quickslice_km.m	Plots as lines Vs at different depths in a transect
resolution_tests_1D_plotall.m	Plots 1D resolution test results
rotate_deg_vs.m	Rotates Vs data files from Cartesian coordinate system to degrees.

Heatflow_Perplex

This looks at heatflow data and uses it to calculate geotherms to use the Perplex analysis done on Siletz-Crescent basalts to decide Vs of Siletzia

heatflowcomp_60to80.m	plots heatflow data from Pollack et al., 1993
heatflow_to_temps.m	Takes heatflow data and calculates geotherm
Perplex_contourplotter.m	Plots Vs with depth and temp from Perplex as a gradient, with forearc geotherm overlaid.
Perplex_Vsplot.m	Plots Vs with depth of Siletzia after all of the above analysis

Phasevel_combine

Combines Helen Janiszewski's regional surface wave EQ phase velocities with ambient noise phase velocities. Described in more detail in Appendix A.3. Main script is **combine2_Helen_**

ANT_EQ.m

SWpackage

Does the surface wave earthquake tomography as described by Jin and Gaherty, 2015. In the directory is a manual **ASWMS_manual.pdf**

extra script to take continuous data in antelope and turn them into the right mat files is **Antelope2Event.m**

Beamforming

Does beamforming, main script is

beamformer1.m

and then the power of the beam over many months is stacked and then plotted

beamformer_power_stack.m

Appendix E.2 GMT plotting codes and other bash scripts

Bash scripts are in /home/kjc233/Documents/data/MSH_ant_2018/

mk_array_map.bash	makes the array map with geology, makes both a local and a zoomed out map of the cascades. geologic features are in the directory /home/kjc233/Documents/data/MSH_ant_2018/plot_feat_deg/
mk_degsvel2_mask.bash	Plots Vs slices with degree coordinates and no drawn on geology features
mk_degsvel_mask.bash	Plots Vs slices with degree coordinates and drawn on geology features
mk_four_deg_error.bash	Plots phase velocity error at three frequencies
mk_four_deg_phvel_feat.bash	Plots phase velocity results at three frequencies with drawn on geological features
mk_kmsurf_input.bash	Makes directories for each pixel labeled y_x to prepare for Vs inversions
mk_kmsvel_nomc_justmap.bash	Makes the maps in km coordinate system for Vs
mk_kmsvel_vsinput.bash	Makes the Vs input files for the plotting
mk_kmsvel_vsinput_med.bash	Makes the Vs input files from the median of many iterations in the MC Vs inversions
mk_kmtransect.bash	Makes transects of Vs model, can do **A** 25 km north of MSH, E-W **B** E-W through MSH and Mount Adams **C** 25 km south of MSH, E-W **D** North-south through MSH

X X-line in Kiser et al., 2016

Y Y-line in Kiser et al., 2016

shebang_MC.bash Runs everything after the inversion up to the transect plots

need to run **rotate_deg_vs.m** in /home/kjc233/Documents/matlab/ANT_plotting/

to rotate km coordinate Vs files to degree Vs files.

Appendix E.3: Location of Data

Seed files:

Long period continuous seismic data is in /ld3/iMUSH/LP/iris

First year of TA and iMUSH station data split up into groups of a couple months is in:

Jul14Sep14three/

Nov14Jan15three/

Jan15Mar15three/

Mar15May15three/

May15Jul15three/

Undecimated (BHZ and HHZ) UW stations:

startHEBO.mseed

endHEBO.mseed

startLEBA.mseed

endLEBA.mseed

startLCCR.mseed

endLCCR.mseed

startRADR.mseed

endRADR.mseed

startKENT.mseed

endKENT.mseed

startSTOR.mseed

endSTOR.mseed

startWISH.mseed

endWISH.mseed

startYACT.mseed

endYACT.mseed

UW stations decimated to LHZ:

HEBO.yr.mseed.resampled

KENT.yr.mseed.resampled

LCCR.yr.mseed.resampled

LEBA.yr.mseed.resampled

RADR.yr.mseed.resampled

STOR.yr.mseed.resampled

YACT.yr.mseed.resampled

WISH.yr.mseed.resampled

Antelope databases:

database for ambient noise lives in /ld3/iMUSH/LP/antelope

and is called **MSH2db**

database for EQ tomography is in **MSHmixdb**

Cross correlation data:

In /home/kjc233/Documents/data/MSHXCresults

MSHjul14jul15UW3pp.mat Cross correlations after stacking

fitxc_jinMSHjul14jul15UW3pp.mat Spectrum fit information

In /home/kjc233/Documents/data/MSH_ant_2018/

There is a directory for each frequency **mhz180** – **mhz050**

in each of these frequency directories there is the station pair-wise phase velocities

mn_phvel_jindd2_0.180.data

renamed to have the frequency name at the end of the file name

Ambient noise 2D tomography data:

In each frequency directory is:

rayinvert_out42.txt	The tomography results
rayinvert_out_42.mat	Tomography results as a mat file
par_iMUSH_42.txt	Parameters used for this result
stat_iMUSH_42.log	Statistics from the inversion that are printed to the screen.

Phase Velocity data of lower frequencies after combining with ambient noise:

In each frequency directory is:

rayinvert_outC.txt	The surface wave tomography with errors scaled 5x, combined with ambient noise at 0.05 Hz, Janiszewski et al., 2018 data at lower frequencies

Vs 3D inversion data

in /home/kjc233/Documents/data/MSH_ant_2018/

surfrun_grad	has inversion results from the gradient model
surfrun_moho	has inversion results from the Moho model

In each directory is:

regEQ.grad.start5 or **regEQ.moho.start5**	the gradient or moho model
period_file	the list of periods used for the synthetic fit
122.5_132.5	The pixel files in km y_x, 75 is added to each so that the names would never be negative
2.5-5.0_km.vs or **2.5_5.0_deg.vs**	The text files with the Vs information with either a Cartesian coordinate system in km or coordinate system

	with degrees. Each has the top and bottom of the layer depth in km as labels.
2.5-5.0_km.nc	GMT readable grid in km coordinate system
2.5-5.0_deg.ps or **2.5-5.0_km.ps**	Plot of Vs depth slice either in km coordinate system or degrees.
Bline.ps	Transect of either A, B, C, or D line.

Inside the pixel directories:

phasevel	The phase velocity data for that pixel
runsurf96.sh	The runfile for the Vs inversion
sr0.01.disp	The phase velocity fit for phasevel
sr0.01.modl	The Vs inversion result for this pixel

all other files are temporary files from each iteration of the Monte Carlo runs.

Network averaged phase velocities and 1D avg Vs:

This data is in /home/kjc233/Documents/data/MSH_ant_2018/startmod_1D

startmod_grad	The 1D avg Vs model run files with a gradient
startmod_moho	1D avg Vs model run files with a Moho
1Dstartmods	Directory with the final 1D avg Vs files which are **regEQ.moho.start5** and **regEQ.grad.start5**
restest_grad	1D resolution test starting models, results, and dispersion fit information for 3 low velocity zones in the crust and upper mantle.
kernel	sensitivity kernel calculations

Appendix E.4: Workflow

Cross correlations

Run the bash script **MatnoiseLoop.bash** which is in /home/kjc233/Documents/data/MSHXCre-sults/

Run this bash script from another directory in /ld3/ because it will save a lot of output.

Then run **mn_add_ncf_stacks2.m** in this same directory where all the batches of mat files are. To get all of these mat files I use the command **glob.m** which is in /home/kjc233/Documents/matlab/. It grabs filenames using wildcards.

Set a new **outfile_prefix** to name the output of the combined batches of cross correlations.

Station pair-wise Phase Velocities

Next run **mn_fitxcspec16.m** to fit the spectrums of the correlograms to get phase velocities. The parameters set at the beginning are the following (in parentheses are what I use):

plot_flag	Plot some examples, set to zero to run all station pairs (0).
ALGORITHM	Set to 1 to fit the spectrum (Jin et al., 2015), to 0 for zero-crossing method (Ekstrom et al., 2009) (1).
fr_max	maximum frequency to analyze (0.25).
order_ampwin	order of polynomial for the smooth Hilbert envelope (5).
SNRmin	Minimum acceptable SNR from input (40).
nmax_zc	Max number of zero crossings saved (25).
vtol	Tolerance on fractional deviation of phase velocity from reference (0.25).
vtol2	Tolerance on fractional change in phase velocity point-to-point (1).
fitctrl	Controls for direct fitting (Amplitude of the polynomial, order of the velocity polynomial, Tolerance in X, Weight for the slope penalty, weight for curvature penalty,vweight for fitting the imaginary part of the spectrum) ([5, 5, 1e-3, 0.01, 1e-4, 0]).

mk_invert_files 1 to output to invertpix format, 0 to not write

vel_bds min and max for phase velocities ([2.0,4.5])

lat_bds station latitude boundaries ([44.8, 47.5]).

lon_bds station longitude boundaries ([-125 -120]).

fref0 frequencies for the reference dispersion curve (should be an array average and should extend beyond what you want as output nodes) ([0.01 0.04 0.06 0.08 0.1 0.12 0.14 0.16 0.18 0.2 0.22]).

phvref0 phase velocities for reference dispersion curve at the above frequency values ([3.6675 3.4935 3.39 3.29 3.24 3.15 3.11 3.06 3.01 2.9671 2.93]).

fknot frequencies at which output phase velocity is calculated (should go below and above what you want as data output for fit stability) ([0.01,0.02,0.04,0.05,0.06,0.08,0.10,0.12,0.14,0.16,0.18,0.2,0.22]).

inpref The name of the mat file input (without the .mat ending) ('MSHjul14jul15UW3pp').

velpref Prefix for the output filename ('mn_phvel_jinF').

Then run **mn_dataselect4.m** to do quality control on the phase velocities.

Input parameters are:

write_on 1 to write output, 0 for testing or plotting.

f Frequency of data ([0.04 0.05 0.06 0.08 0.1 0.12 0.14 0.16 0.18]).

lowcut Cutoff for minimum number of cylces at each frequency ([1 1 1 2 2 2 2 2 2]).

highcut Cutoff for maximum number of cycles at each frequency ([5 5 5 5 5 5 5 5 5]).

yplot 1 to plot things, 0 to run quickly

In the textread command, set the correct name prefix within sprintf for the input phase velocity files.

outtextfile set the correct prefix within sprintf for the output phase velocity filename

Copy these files into directories with the frequency names in mhz (**mhz180 – mhz050**).

Examples in /home/kjc233/Documents/data/MSH_ant_2018/.

Data columns of these phase velocity files are Lat (station 1), Lon (station 1), Lat (station 2), Lon (Station 2), Phase Velocity (km/s), Uncertainty (km/s), Distance between stations (km), Average wavelength (km), Station Pair Name.

2D Ambient Noise Tomography

Run **loop_iMUSH_rayinvert.m** in directory above all the frequency directories (**mhz180 – mhz050**).

parameters to set are:

rnum Run number, used to save unique file names.

parfile set name within sprintf of the parameter file

statfile set name within sprintf of the statistics file (stuff printed to screen).

outfile set name of output text file of velocity tomography within sprintf.

outputmat set name of output mat file within sprintf.

xxmin minimum x value in km for output files (-75).

xxmax maximum x value in km for output files (75).

yymin minimum y value in km for output files (-75).

yymax maximum y value in km for output files (75).

stafile station information file (lat, lon, elev, etc.) ('../stalist_mshall.txt')

[dirs,isdir] directory names of frequency directories with data (**mhz180 – mhz050**), used **glob.m** (in /home/kjc233/Documents/matlab/) to grab them all using wildcards. isdir is just 1 if it is a directory and 0 if it is a file (not used).

prior_all smoothing parameter in order of increasing frequency , glob grabs directories for frequencies that are for surface wave earthquake data but these are skipped in the loop and the prior_all is just set to a dummy variable 1. ([1 1

	1 1 0.0121 0.015 0.0208 0.0267 0.0325 0.0383 0.0442 0.05]).
priordatall	uncertainty error scaling factor in order of increasing frequency. ([1 1 1 2 4.32 7.68 3.5 6.44 6.44 6.44 5.03 5]).
latref	latitude where y =0 (46.2).
lonref	longitude where x=0 (-122.18).
azref	rotation of the coordinate system (0).
xmin	minimum x value of the coordinate system (-140).
xmax	maximum x value of the coordinate system (140).
ymin	minimum y value of the coordinate system (-200).
ymax	maximum y value of the coordinate system (200).
dxy	x and y interval (5).
vref	reference velocity, used to rescale smoothing from velocity to slowness. (2.9).
reslvl	Resolution kernel diagonal value used to draw a contour on tomo (0.1).
dosmooth	1 to treat smoothing parameter as 1st derivative smoothing, 0 to treat as norm damping (1).
doresvar	1 to calculate resolution and variance, 0 to skip (1).
ffrqmode	0 uses ray theory, >0 gives the # of Fresnel zones in approximation of finite frequency kernels (2).
priorfac	additional norm damping. Multiplies priorfac by 1/priormod^2 and adds to the diagonals of the kernel (0.1).
[datafile, isdir]	name of the data files, using **glob.m** again with the data file name prefix and a wildcard.

Can plot the tomography results using **mk_four_deg_phvel_feat.bash** to make a figure like Figure 2.6. The phase velocity error plots like Figure 2.3 are made with **mk_four_deg_error.bash.**

Network Average 1D Vs Model

The average phase velocities are calculated in **rayinvert_cp.m** and each average phase velocity

and uncertainty for each frequency is saved as avgstd.txt in each frequency directory **mhz180 – mhz050**. Rewrite each of these into one avgphasevel file in writedisp_surf96.m format.

An example of solutions for the 1D average Vs model is in /home/kjc233/Documents/data/MSH_ant_2018/startmod_1D/startmod_grad /

need the following files in this directory:

grad.start4 A starting model

period_file A file with all of the periods

0.00_0.00 A directory with the following files:

avgphasevel a phase velocity file with the average velocities in write-disp_surf96.m format

Then run **invert1d_montecar_msh_1D_grad.m** in the directory above **0.00_0.00** and you will get the dispersion curve fit sr0.01.disp and the model sr0.01.modl.

To plot the average dispersion curve and 1D starting model like in Figure 2.2 just run **plot_surf96_disp_model_output4.m**

The sensitivity kernels in Figure 2.2 are calculated in /home/kjc233/Documents/data/MSH_ant_2018/startmod_1D/kernel

You need the following files in this directory:

sobs.d with the starting model name as the third line, this should be the normal starting model but interpolated to have twice as thin of layers, and all the same layer size down to the halfspace. The fourth line is avgphasevel2, which it doesn't matter what the phase velocities are, but it should have one period, one line, and calculate the kernel at one period at a time. Also it has to be U, group velocity, not C, phase velocity for some reason.

avgphasevel2 One line, with one period, any group velocity and the third column should be U not C. Calculate one period at a time.

startmod.interp2 The starting model interpolated for much thinner, even layers.

Then run the following sequence for each period:

surf96 39

surf96 1

srfker96 > srfkernel.txt

surf96 39

Give the file names srfkernel.txt unique names for each period, in a way that ls would list them in increasing or decreasing order with period for ease of plotting. Plot them with **sensitivity_ker_plot.m**

Vs Inversions

Use **mk_kmsurf_input.bash** within a new directory that has the starting model to make each pixel directory , named y_x, with the dispersion curve data in each directory.

Change

filename to ../mhz*/[name of phase vel file] (../mhz*/rayinvert_outC.txt)

filename2 to [name of phase vel file] (rayinvert_outC.txt)

startname to name of starting model (../regEQ.moho.start5)

Where **x** and **y** are defined, add a number so that the directory names are never negative, I added 75.0 since the minimum value of x and y is -75. Linux has a hard time with directory names that start with a "-".

Add a file called **period_file** that lists all the periods in decreasing order (example in **surfrun_grad**). This is used to calculate synthetic fits to the starting model.

Now run **invert1d_montecar_msh_1D_grad.m** if using the gradient model or **invert1d_montecar_msh_1D_moho.m** if using the moho model within the directory with all the pixel directories. Parameters to set are:

modfile	name of starting model (‘regEQ.grad.start5’).
dispfile	name of phase vel data file (‘phasevel’).
alloutfile	name of output mat file (‘allmodels.mat’).
textoutfile	name of output text file (‘allmodels.txt’).
period_file	name of file with list of periods used (‘period_file’).
isfigure	whether or not to plot things for debugging (0).
isdebug	can just do a couple pixels for debugging (0).
dep_knots	depth knots where starting model is perturbed ([0 5 10 20 35 60 max(vec_dep)+vec_h(nlyrs-1)]).
dirlst	String name with wildcards to grab all pixel directories **(**dir(‘*.5_*.5’));
pixlist	If in debug mode, list names of pixels you want to do a test inversion on.

More parameters are set in **setup_parameters_msh.m**

testN	number of MC iterations (100).
velocity_var	variance of velocity perturbations (0.1).
r	allowed std of output (0.2).

Run this inversion a second time with **dep_knots** set to staggering values from the first ru n. Ex. ([0 2.5 7.5 15 27.5 47.7 87.5 max(vec_dep)+vec_h(nlyrs-1)]). Then average the two runs to give smooth uncertainty values (running just once give big lobes in the uncertainties).

To plot the Vs output run **shebang_MC.bash** which runs

mk_kmsvel_vsinput.bash	Makes Vs files per depth slice, need to set start model file name in the beginning.
mk_kmsvel_nomc_justmap.bash	Plots the Vs maps in the Cartesian coordinate system.
mk_kmtransect.bash	Plots the transects, need to set which transect to plot in the beginning (A,B,C, D, X, or Y). Need to write a list of GMT

grid files (.nc) in order of increasing depths and set as the variable **file.**

mk_kmtransect.bash makes transects like in Figure 2.10 and Figure 2.11.

Rotate the Vs text files from Cartesian to degrees by running **rotate_deg_vs.m**

Then run **mk_degsvel_mask.bash** to plot the Vs maps in degrees as in Figure 2.8.

For Figure 2.10 the E and W avg Vs comparison plots are made with **EW_compare_Vs.m,** And the Vs line plots with depth are made with **quickslice_km.m.**

Figure 3.1 is made with **Perplex_Vsplot.m.**

Resolution Tests

2D tomography resolution tests

Can do checkerboard tes or test a single block by setting iblob to 0 or 1 respectively in **fwdmod_synth.m** Can set the following parameters for the tests

grd	checkerboard block size in pixels
per	percent deviation in velocity of blocks
width	width of block
height	height of block
xcen	center of block (x) in km
ycen	center of block (y) in km
isneg	block is negative anomaly if 0 and positive if 1

Running the tests gives a mapview of the solutions to make figures like Figure 2.5. To make a transect figure like Figure 2.4, run **resolution_2D_lineplot.m** after loading the mat file with all the resolution tests at all frequencies.

1D Vs resolution tests

in /home/kjc233/Documents/data/MSH_ant_2018/startmod1D/restest_grad/

is a bash script called **restest_noise.bash**

in **synthetic.bash** set the first file read in to be the model with the perturbation you are testing, here it is set to LVZ.three.start. Need a file called period_file with a list of periods. Need a file

read by surf96 called **sobs.d** which has the starting model as the third line and the synthetic phase velocity file as the fourth line (phasevel_synth_unc is the name of the file written by restest_noise.bash). This outputs a fit of the synthetic phase velocity as sr0.01.disp and the Vs model as sr0.01.modl. Can make a nice plot like Figure 2.7 by running **resolution_tests_1D_plotall.m**